Wind Tunnel Assessment of a Robust Gust Load Alleviation Controller Designed Using μ-Synthesis

Felix Stalla*, Gertjan Looye†, Thiemo M. Kier‡, Kolja Michel§
Institute of System Dynamics and Control, German Aerospace Center (DLR), 82234 Weßling, Germany

Thomas G. Schmidt¶, Charlotte Hanke‖
Institute of Aeroelasticity, German Aerospace Center (DLR), 37073 Göttingen, Germany

Tania Kirmse**
Institute of Aerodynamics and Flow Technology, German Aerospace Center (DLR), 37073 Göttingen, Germany

Manuel Pusch††
Munich University of Applied Sciences, 80335 Munich, Germany

Gust and turbulence loads are a sizing case in the structural design of a transport aircraft, particularly for those with high aspect ratio wings. Active control technologies can help reduce these loads, leading to a lighter aircraft design, which in turn reduces fuel consumption and emissions. Robust control is a well-suited method to develop controllers for the multi-variable aeroservoelastic system, with μ-synthesis providing explicit treatment of system uncertainties to guarantee robust performance and stability. However, applying μ-synthesis presents the challenge of translating the desired control objectives into the synthesis framework that includes a generalized plant and weighting functions. This paper addresses this challenge in the context of designing a gust load alleviation controller, which is intended for experimental testing in a wind tunnel. The goal is to demonstrate the practical applicability of the μ-synthesis method and to develop a guideline for controller design. Competing control objectives, such as performance, control effort, and robustness, will be explicitly addressed and balanced within the design process. The benefits of μ-synthesis for controller design in multi-variable systems are explored by comparing three different controllers, each utilizing different subsets of sensors and actuators. The developed controllers are experimentally validated by wind tunnel testing.

I. Introduction

Future commercial aircraft will be equipped with high-aspect ratio wings designed for optimized induced drag. These wings will feature a slender design and greater flexibility, increasing the loads induced by gusts and turbulence. Active control technologies can help to limit these resulting loads, enabling a lighter structural design with a positive effect on weight, emissions, and fuel economy [1].

Load alleviation systems are already implemented on numerous military and passenger aircraft, like the Northrop B-2, Lockheed L-1011, Boeing 787, and all Airbus aircraft since the development of the A320, see also [2]. Most of these load alleviation systems are based on the acceleration measured within the aircraft's fuselage, thus concentrating on rigid body motion and alleviating loads by adding a load-factor control functionality to the primary flight control system [2, 3]. A current focus in research is the use of distributed sensors that allow to specifically address the flexible motion of the wings, and hence the occurring loads, where loads at the wing-root play a key role. Another development is the addition of feedforward control by means of a LIDAR sensor or an angle-of-attack vane [4], however this paper will be focused on feedback control for gust load alleviation (GLA).

The design of a gust load alleviation controller poses a multi-variable output feedback problem, since the aeroservoelastic system features several control effectors (ailerons, flaps, spoilers, elevators) and sensors (acceleration, load estimation), which can only capture part of the states. A range of controller design methods have been applied to

*Research Associate, felix.stalla@dlr.de.
†Department Head, gertjan.looye@dlr.de, AIAA Member.
‡Research Associate, thiemo.kier@dlr.de, AIAA Member.
§Research Associate, kolja.michel@dlr.de.
¶Research Associate, tg.schmidt@dlr.de.
‖Research Engineer, charlotte.hanke@dlr.de.
**Research Associate, tania.kirmse@dlr.de.
††Professor, manuel.pusch@hm.edu.

the load alleviation problem. Classical methods like a linear-quadratic-Gaussian (LQG) regulator [5] necessitate the tuning of both a controller and a Kalman filter to deal with output feedback. Furthermore, using a LQG regulator creates challenges in guaranteeing stability margins. Other methods such as collocated control [6] are simple to implement but lead to an unnecessary reduction of the solution space of the multi-variable problem by fixing input-output relations within the controller. Modern methods are for example dynamic inversion [7] and model-predictive control [8]. Dynamic inversion can ideally compensate gust disturbances by inverting the plant dynamics, however this inversion is challenging for a high-order aeroelastic system. Model-predictive control adapts its control law during execution and can take actuator constraints into account, but is computationally more demanding when executing the control law.

Robust control [9, 10] is a well-suited control method for application to an aeroservoelastic system, yielding an optimal solution to the problem of connecting control inputs and outputs, while simultaneously addressing objectives like performance, control activity, and robustness. A generalized plant, along with weighting functions, is defined to translate the control objectives into a synthesis problem. This approach abstracts the problem to a higher-level formulation, rather than directly tuning the controller gains. All objectives must be reflected in the H_∞-norm of the closed-loop system, which is shaped during the synthesis.

Unlike pure H_∞-norm shaping, which mandates robustness requirements to be specified by an additional weighting function, μ-synthesis (also called D-K-iteration) [9, 11] allows robustness requirements to be incorporated directly through an uncertain model. The uncertain model is created by introducing structured or unstructured uncertainties into the plant's transfer matrix. Structured uncertainties are applied to specific elements or parameters of the plant, such as actuators or sensors, whereas unstructured uncertainties are lumped at the plant's inputs or outputs [9]. For an aeroservoelastic system, the uncertainties reflect varying operating conditions, degrading properties of sensors and actuators, or neglected dynamics. μ-synthesis ensures a functional controller with guaranteed performance and stability, even in the presence of the defined uncertainties [9].

The key challenge in robust control is setting up the generalized plant, defining its input and output channels, and selecting appropriate weighting functions for these channels, to accurately reflect the control objectives. In μ-synthesis, an additional challenge is the definition of the uncertain model. This is not always intuitive, and the result of the synthesis is highly dependent on the defined setup. This paper addresses this challenge in the context of applying μ-synthesis in controller design for gust load alleviation. A guideline is developed on how to select the weighting functions to achieve the desired load reduction, while balancing performance with control activity as well as stability and robustness. Robustness requirements are incorporated by defining structured uncertainties in actuators and sensors.

One advantage of robust control is the ability to define control objectives at a higher level. This paper explores this benefit by comparing three different controllers, each using a distinct subset of actuators and sensors, keeping the higher-level objectives identical. This demonstrates the adaptability of the synthesis setup. The developed GLA controllers are validated experimentally in a wind tunnel campaign, the setup is depicted in Fig. 1.

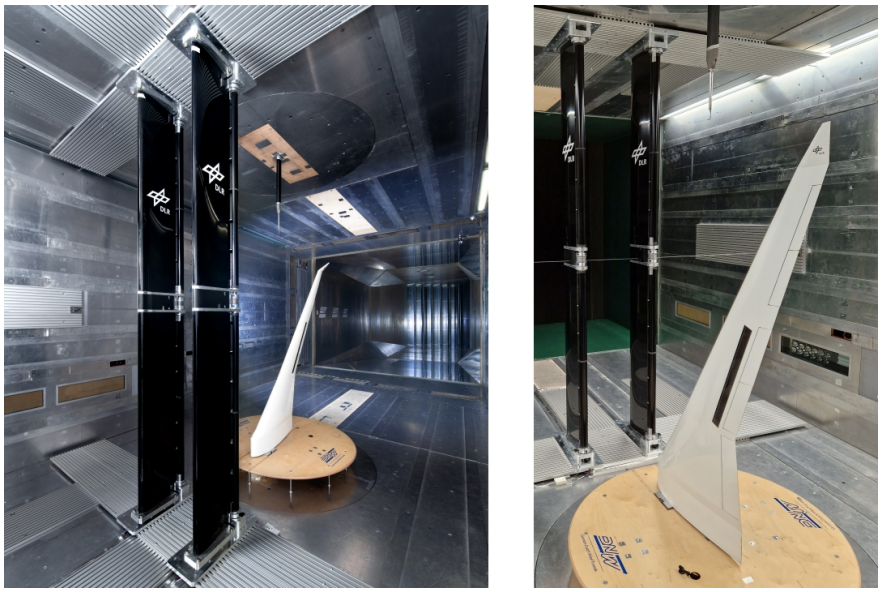

Fig. 1 Experimental setup of the oLAF wind tunnel test, with gust generator and flexible wing.

The experiment was conducted in the low speed wind tunnel Braunschweig (DNW-NWB) within the optimally Load-Adaptive Aircraft (oLAF) project of the German Aerospace Center (DLR). The oLAF experimental wing is derived from a long-range civil aircraft, exhibiting sweep and an aspect ratio greater than ten. For load alleviation, five trailing edge control surfaces are installed (visible on the right in Fig. 1), and ten acceleration sensors at multiple spanwise locations complete the feedback loop. A gust generator is installed upstream of the wing, shown as the black structure in Fig. 1. This device features slotted rotating cylinders, allowing to introduce continuous as well as discrete gusts at a defined frequency. A five-hole-probe attached at the wind tunnel ceiling provides measurements of the gust angle. More information on the oLAF wind tunnel experiment can be found in [12]. The development of the flexible wing and the gust generator concept are described in [13] and [14], respectively.

This paper focuses on demonstrating the applicability of μ-synthesis for robust gust load alleviation, but also demonstrates the effectiveness of active load alleviation. Section II describes the simulation model of the aeroservoelastic wing used for controller design. The structural dynamics, aerodynamics, actuator dynamics, and sensor properties are identified separately at the beginning of the wind tunnel campaign, and combined into an integrated aeroservoelastic model used for (re)-synthesizing the controller. Further information on modeling and parameter identification is given in [15] and [16]. Section III describes the application of μ-synthesis to design the GLA controller for the wind tunnel experiment. Following an introduction of the method, the choice of the generalized plant, weighting functions, and uncertainty models are presented. Three controller variants with the same control requirements but different sensors and control surfaces are designed and compared in simulation in Section IV. Robustness is investigated by disk-based stability margins and μ-analysis. Section V presents the wind tunnel experimental assessment of the designed controller variants. The experiment evaluates the reduction in wing-root loads as well as the control action, for multiple frequencies of gusts. The gusts are applied both continuously (sine-like) and discrete (1-cos-like). Promising results for gust load alleviation could be achieved.

II. Aeroservoelastic Modeling and Parameter Identification

The gust load alleviation controller is designed using a numerical model of the aeroservoelastic wing. A nonlinear simulation is set up to validate the controller prior to entering the wind tunnel, while a linear state-space model is used in controller synthesis. The modeling procedure follows [17] and employs the VarLoads environment [18, 19] to set up a structural and an aerodynamic model, which are combined by aero-structural interaction and appended by actuators, sensors, and load recovery computations to virtually represent the oLAF wind tunnel model. Figure 2 schematically depicts the modeling procedure. Here, only a brief summary of the numerical model will be given, a comprehensive description of the modeling is outlined in [15].

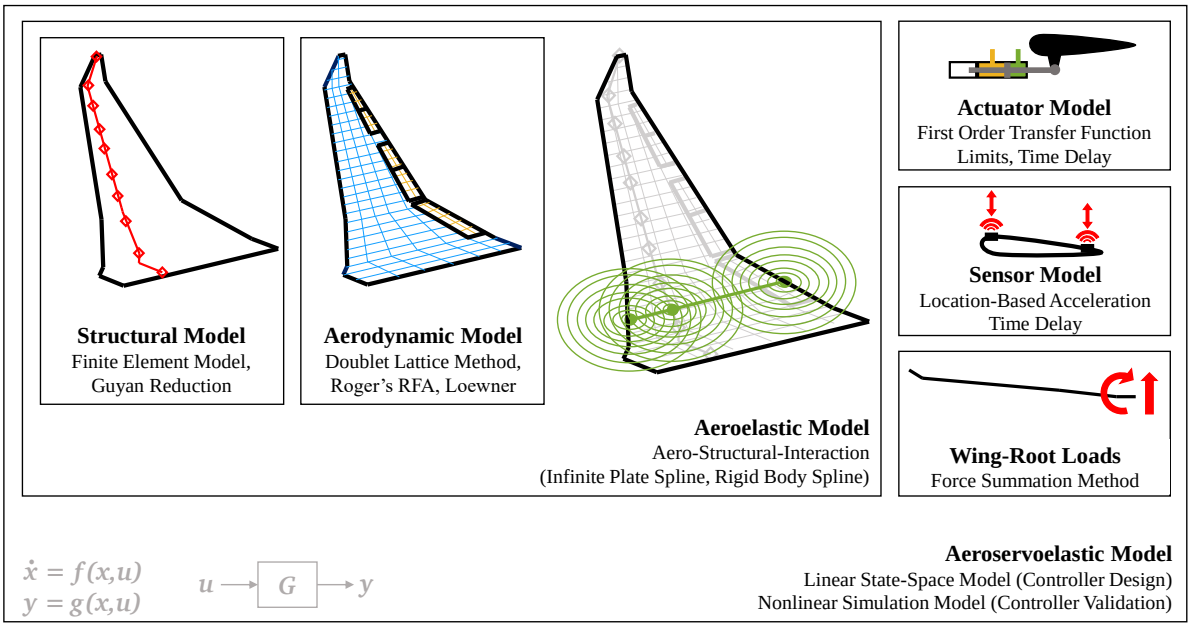

Fig. 2 Schematic representation of the numeric modeling process.

A. Numerical Aeroservoelastic Model

Structural dynamics form the baseline of the aeroservoelastic model, using the linear elastic equations of motion (EOM) in mean-axes coordinates [20, 21]. In this equation, the modal matrices of stiffness $\mathbf{K}_{ff}$, damping $\mathbf{B}_{ff}$, and mass $\mathbf{M}_{ff}$ are obtained from a Guyan reduced [22] finite element model by modal analysis. More information on the finite element model of the oLAF flexible wing can be found in [13]. The subscripts are in accordance with the Nastran Aeroelastic User Guide [23]. The forces and moments $\mathbf{P}_g^{\text{ext}}$ on the right side of the equation excite the system, and stem from aerodynamics and gravity. Since the wing is clamped in the wind tunnel experiment, there are no rigid body dynamics except for an enforced pitch angle. The modal analysis also yields the eigenvectors of the undamped system, which are combined in the matrix $\mathbf{\Phi}_{gf}$, yielding the EOM, in which $\mathbf{u}_f$ denotes the modal displacement:

$$\mathbf{M}_{ff} \cdot \ddot{\mathbf{u}}_f + \mathbf{B}_{ff} \cdot \dot{\mathbf{u}}_f + \mathbf{K}_{ff} \cdot \mathbf{u}_f = \mathbf{\Phi}_{gf}^T \cdot \mathbf{P}_g^{\text{ext}}. \tag{1}$$

The aerodynamic forces are calculated by a doublet lattice method (DLM) on the discretized wing surface. For each panel, the local pressure coefficient $\mathbf{\Delta c}_{p,j}$ is calculated by multiplying the downwash $\mathbf{w}_j$ induced on the respective panel with the aerodynamic-influence-cofficient (AIC) matrix $\mathbf{Q}_{jj}$. To obtain loads, the pressure coefficients are multiplied by dynamic pressure q_∞, the matrix $\mathbf{S}_{kj}$, and the aero-structural coupling matrix $\mathbf{T}_{kg}$. The latter is derived by coupling aerodynamic and structural model employing rigid body splines [24] and infinite plate splines [25]. Hence, the following equation can be written describing the aerodynamic forces and moments:

$$\mathbf{P}_g^{\text{aero}}(k) = q_\infty \cdot \mathbf{T}_{kg}^T \cdot \mathbf{S}_{kj} \cdot \underbrace{\mathbf{Q}_{jj}(k) \cdot \mathbf{w}_j}_{\mathbf{\Delta c}_{p,j}}, \qquad k = \frac{\omega \cdot c_{\text{ref}}}{2 \cdot U_\infty}. \tag{2}$$

The DLM computes the aerodynamics in the frequency domain, which is why the forces and moments depend on the reduced frequency k [26]. The reduced frequency can be computed from the radial frequency ω of the harmonic motion, the reference length c_{ref}, and the freestream velocity U_∞. Roger's rational function approximation (RFA) [27] and the Loewner framework [28] are used to transfer the aerodynamics to the time domain. The input in Eq. 2 is the downwash $\mathbf{w}_j$. This downwash is generated by the flexible motion of the wing, a deflection of the control surfaces, or the gust disturbance acting on the wing. In the wind tunnel experiment the gusts will be injected into the airflow by the gust generator shown in Fig. 1. Therefore it is chosen to adapt the definition of the 1-cos discrete gusts detailed in the certification documents [29] to a more open definition of the gust amplitude α_G:

$$w^G(t) = \begin{cases} \alpha^G \cdot \left(1 - \cos\left(\frac{2\pi \cdot U_\infty \cdot t}{2 \cdot H}\right)\right) & t_s \leq t \leq t_e, \\ 0 & \text{otherwise.} \end{cases} \tag{3}$$

In above's formula, the gust gradient is denoted H, the freestream velocity U_∞, and the time t with the according start time t_s and end time t_e of the gust interaction. The gust gradient H depends on the frequency of rotation of the generator and the resulting frequency of the gust f^G, following the relation $H = U_\infty / 2 f^G$.

Having built the aeroelastic model, the addition of actuators, sensors, and a load recovery calculation yield the aeroservoelastic model, see Fig. 2. The oLAF experimental wing features five trailing edge flaps as depicted in Fig. 3, each driven by the same actuator type. Ten acceleration sensors at multiple spanwise locations provide information for feedback control. The sensors are placed in pairs at each spanwise location, one near the leading edge, one near the trailing edge. This allows a reconstruction of the torsional motion, while out of plane-bending is directly captured.

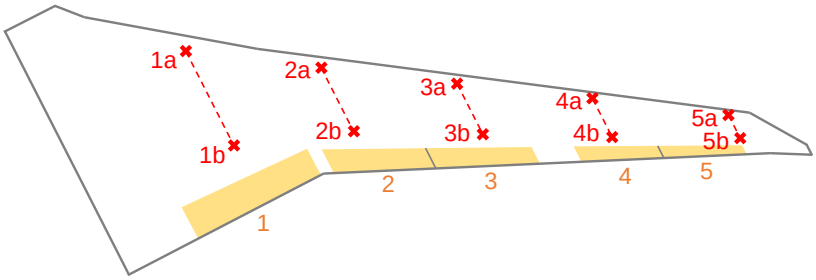

Fig. 3 Position and ID of the control surfaces and acceleration sensors on the oLAF wing.

The actuators are defined by a first order transfer function with added time delay and limits in deflection, rate, and acceleration, as proposed in [30]. The non-linearities of the limits are only present in the simulation environment for controller validation, while the state-space model for controller synthesis is purely linear. The acceleration sensors are modeled by rigid body splining [24] from the condensed structural model to the location of the respective sensor. The sensors can only capture the acceleration in the upward (out-of plane) direction. Time delay is also added to the sensor model. The wing-root loads are recovered by the force summation method (FSM) [17], yielding the wing-root bending moment (WRBM) and wing-root torsion moment (WRTM), which are the primary target for load alleviation.

B. Parameter Identification and Numerical Model Validation

Before commencing with the wind-tunnel tests, the oLAF experimental wing is identified, in order to update the numerical model introduced above and to re-tune the designed controllers. The model components, namely structure, actuators, and sensors, are identified separately and each component is updated in the numerical model. The aerodynamics cannot be identified separately, which is why the final step of the identification procedure is to check the agreement of numerical model and experimental data for the coupled aeroservoelastic system. The identification and model update procedure is presented in detail in [16].

The structural parameters are identified by releasing the model from a static deflection created by applying a unit force near the wing tip. This allows to identify the eigenfrequency of the first flexible modes, which can then be used for a finite element model update. This leads to an updated model mass and stiffness matrix. The damping matrix - which is modeled as stiffness- and mass-proportional [26] - is also updated by analyzing the decay of the oscillation in the experimental setup. The modification is related to the first and second flexible mode only. For GLA controller design, these modes are the most important ones.

Actuators are identified by measuring the actual deflection given a commanded deflection. This allows to determine the first order linear transfer function, i.e. the roll-off frequency ω_0, as well as the time delay in the actuation system. The limitation in deflection is given by the geometry of the experimental wing, allowing the control surfaces to deflect 14° in either direction. Limitations in rate and acceleration are not identified for the oLAF wing, but taken from [30], in which a similar actuator was identified.

Sensors are identified regarding their noise properties, as this allows to select appropriate filters for the GLA controller to be designed. Both low frequency bias as well as high frequency noise is observed. An overview of all identified quantities leading to an updated numerical model is given in Table 1.

Table 1 Model parameters used in the updated numerical model.

Domain	Parameter	Symbol	Value	Source	Comment
structure	1st flex. eigenfreq.	$f_{\text{eig},1}$	8.5 Hz	identified	out-of-plane bending
	2nd flex. eigenfreq.	$f_{\text{eig},2}$	36.5 Hz	identified	out-of-plane bending
	damping correction factor	k_{b}	0.8	identified	correcting the first entry in $\mathbf{B}_{ff}$
actuator	roll-off frequency	$\omega_{0,\text{act}}$	14.5 Hz	identified	first order model
	dead time	$T_{\text{d,act}}$	6.0 ms	identified	-
	deflection limit	δ_{max}	±14°	geometric	-
	rate limit	$\dot{\delta}_{\text{max}}$	$\pm 1130°/s$	from [30]	-
	acceleration limit	$\ddot{\delta}_{\text{max}}$	$\pm 79500°/s^2$	from [30]	-
sensor	noise std. deviation	σ_{n}	0.75 m/s²	identified	with actuators on

Having updated the structural, actuator, and sensor model, the only uncertainty remaining stems from aerodynamics and the aero-structural coupling. The updated model is therefore compared with experimental data obtained in an aeroservoelastic characterization. For controller design it is important to correctly capture the transfer behavior from the inputs - a gust disturbance and the control surface commands - to the ouputs - the acceleration sensors and the wing-root loads measured at the wind tunnel balance. Figure 4 shows the transfer function from a commanded deflection on each trailing edge flap to the WRBM, for a freestream velocity of 30 m/s. The faded lines represent the identified behavior from experimental data, the solid lines represents the simulated frequency response. The dynamic measurements are obtained by a frequency sweep from 0 to 12 Hz with an amplitude of 6°. These are corrected in magnitude to the level of WRBM that is achieved when the flap is statically deflected. Note that flap 2 was inoperable during the wind tunnel test.

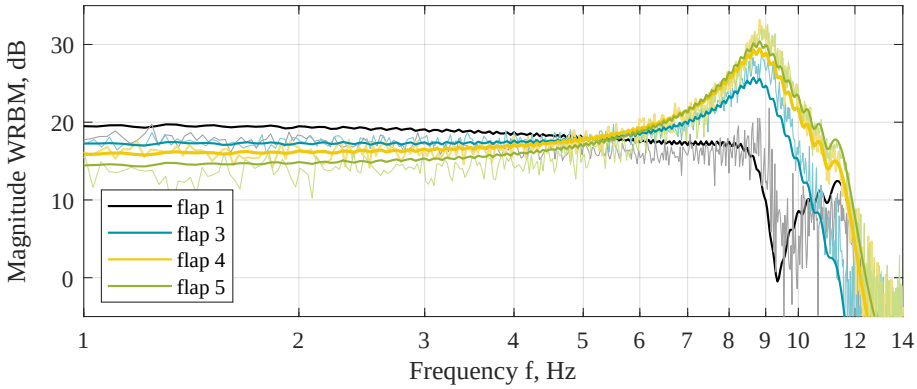

Fig. 4 Identified and simulated transfer function from flap commands (6° amplitude) to WRBM, at 30 m/s.

The simulated and experimentally identified transfer functions match well, up to the limit in frequency of 12 Hz until which the identification is carried out. The peak in the transfer function is clearly visible at about 9 Hz. This is the first bending mode of the coupled aeroservoelastic system, at a freestream velocity of 30 m/s. Similar analyses and comparisons are performed for the transfer functions between the control surfaces and other loads and the acceleration sensors. Additionally, the transfer function from a gust input to loads and acceleration is investigated. The results are satisfactory, and a good match between numerical model and experimental data is obtained, see [16] for details. As the controller is designed using the numerical model, the match of model and experimental data is of importance.

Besides the information on model validation, Fig. 4 indicates the control surface effectiveness with respect to the loads that shall be addressed by the GLA controller. In the low frequency regime, i.e. the static case, flap 1 (most inboard) produces the highest bending moment. This is due to the large size of the surface and its location near the wing root, where the aerodynamic lift is high. More outboard control surfaces benefit from an increased lever arm, but experience reduced lift as they are closer to the wingtip, while being smaller in size. In the dynamic case however, the effectiveness of the flaps is widely different. At the first flexible eigenfrequency of about 9 Hz, flap 5 (most outboard) produces the highest WRBM. Flap 4 generates a similar magnitude. Meanwhile, flap 1 is significantly less effective. Therefore, for GLA in the regime of the first eigenfrequency, flaps 4 and 5 seem to be most effective, which will be considered in controller design in the next section.

III. μ-Synthesis for Gust Load Alleviation Controller Design

Robust control using μ-synthesis is a well-suited method to design controllers for aeroservoelastic systems, as introduced earlier. The primary challenge is translating the control objectives into the synthesis problem setup. First, a generalized plant must be constructed, with exogenous inputs and outputs. Second, the generalized plant is augmented with weighting functions and uncertainties, chosen to meet the control objectives. These two steps are often not intuitive, which is why this section aims to provide a guideline for controller designers on how to perform these steps. Inspiration is taken from [31], but extended to μ-synthesis with an uncertain plant. The application is the GLA controller design for the wind tunnel experiment, though the framework can be adapted to other aeroservoelastic problems. Subsection III.A will review the most important concepts of μ-synthesis, Subsection III.B will develop the generalized plant including uncertainties, and Subsection III.C will provide a guideline for selecting the weighting functions.

A. Theoretical Background

The μ-synthesis method, also referred to as D-K-iteration [9, 11], is a multiple input multiple output (MIMO) robust optimal control technique based on shaping the closed-loop transfer function of an uncertain system. It is an extension to H_∞-synthesis [10], combining it with μ-analysis using the structured singular value (SSV) μ [32] - from which the name of the synthesis method is derived. The objective of μ-synthesis is to achieve robust performance [11] for the controlled system, i.e. meeting defined closed-loop requirements while being robust against uncertainties. Uncertainties arise due to assumptions, unknowns, or unmodeled dynamics in the controller design model, as well as deviating operating conditions and disturbances.

The algorithm looks for an optimal controller applying H_∞-synthesis (K-step), while making sure that sufficient stability margins are kept, taking the pre-defined uncertainties into account. This is ensured by performing a μ-analysis and scaling the plant used for controller design (D-step). D- and K-steps are executed in alternating fashion, until a controller is found fulfilling both performance and robustness requirements. The combination of synthesis and analysis however leads to the loss of joint convexity, potentially yielding a non-global optimum for the controller [9].

A standardized interconnection structure for plant and controller is established in robust control [9], as depicted in Fig. 5 below. The generalized plant **P** - which will be introduced in the next section - with exogenous inputs **w** and outputs **z** is interconnected by the controller **K** with feedback variables **v** and control variables **u**. The structure is appended by uncertainties within the **Δ**-matrix, interconnected with the plant by uncertainty inputs $\mathbf{u}_\Delta$ and outputs $\mathbf{y}_\Delta$. The definition of uncertainty is done on individual elements or signals of **P**, and then cast into the depicted structure.

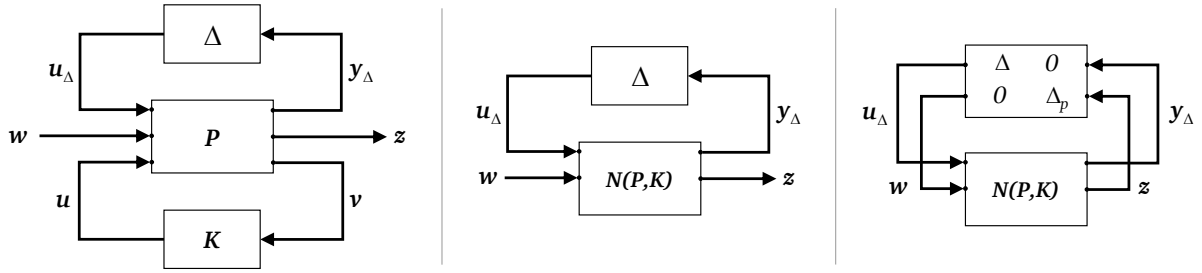

Fig. 5 Standard robust control framework in three formulations, adapted from [9].

Applying a lower linear fractional transform (LFT), the plant-controller-interconnection can be formulated as $\mathbf{N}(\mathbf{P}, \mathbf{K})$, as depicted in the center in Fig. 5, while an upper LFT formulates the interconnection of the generated closed-loop system $\mathbf{N}(\mathbf{P}, \mathbf{K})$ with the uncertainty matrix **Δ**, here denoted as $\mathbf{F_u}(\mathbf{\Delta}, \mathbf{N}) = \mathbf{F_u}(\mathbf{\Delta}, \mathbf{P}, \mathbf{K})$. The resulting block diagram of the upper LFT is not depicted in Fig. 5. It holds [9]:

$$\begin{aligned} \mathbf{N} = \mathbf{F}_l(\mathbf{P}, \mathbf{K}) &= \mathbf{P}_{11} + \mathbf{N}_{12}\mathbf{K}(\mathbf{I} - \mathbf{P}_{22}\mathbf{\Delta})^{-1}\mathbf{P}_{21}, \\ \mathbf{F}_u(\mathbf{N}, \mathbf{\Delta}) &= \mathbf{N}_{22} + \mathbf{N}_{21}\mathbf{\Delta}(\mathbf{I} - \mathbf{N}_{11}\mathbf{\Delta})^{-1}\mathbf{N}_{12}. \end{aligned} \tag{4}$$

Closed-loop shaping (K-step) employs the H_∞-norm [10] of the dynamic transfer function $\mathbf{N}(\mathbf{P}, \mathbf{K})$ in MIMO form:

$$\|\mathbf{N}(s)\|_\infty = \sup_\omega \bar{\sigma}(\mathbf{N}(j\omega)), \tag{5}$$

indicating the maximum value of the largest singular value $\bar{\sigma}$ over the frequency range ω. As the name suggests, the structured singular value μ also plays an important role in μ-synthesis. Using a general formulation assuming the uncertain plant is labeled **M**, the structured singular value is defined as [32]:

$$\mu_{\mathbf{\Delta}}(\mathbf{M}) = \left[\min_{\mathbf{\Delta}} \{\bar{\sigma}(\mathbf{\Delta}) \mid \det(\mathbf{I} - \mathbf{M}\mathbf{\Delta}) = 0\}\right]^{-1}, \quad \text{for } \mathbf{\Delta} = \text{diag}[\mathbf{\Delta_1}, ..., \mathbf{\Delta_m}], \quad \bar{\sigma}(\mathbf{\Delta_i}) \leq 1 \; \forall i, \tag{6}$$

meaning the value μ is the reciprocal of the maximum singular value $\bar{\sigma}(\mathbf{\Delta})$ of the smallest uncertainty matrix **Δ** that renders the closed-loop uncertain system singular. The importance here is the block diagonal structure present in the uncertainty matrix **Δ**, as this structure effects the singular value. The block diagonal elements $\mathbf{\Delta}_i$ can also be single values, then often written as $\delta_i \cdot \mathbf{I}$. If no structure is present in **Δ** then μ and $\bar{\sigma}$ have the same value.

The SSV can be applied in μ-analysis [32] to assess performance and stability of the closed-loop system. Uncertainty needs to be defined on signals and elements of **P**, which can then be formulated as a **Δ**-matrix as shown in Fig. 5, with properties of **Δ** given in Eq. 6. The following definitions hold for the closed-loop uncertain system **N** that is internally stable, with the general matrix **M** in Eq. 6 replaced by the respective quantity [9]:

$$\begin{aligned} &\text{Nominal Performance} && \mu_{\mathbf{\Delta}_p}(\mathbf{N}_{22}) < 1, \; \forall\omega, \\ &\text{Robust Stability} && \mu_{\mathbf{\Delta}}(\mathbf{N}_{11}) < 1, \; \forall\omega, \\ &\text{Robust Performance} && \mu_{\tilde{\mathbf{\Delta}}}(\mathbf{N}) < 1, \; \forall\omega, \quad \text{with } \tilde{\mathbf{\Delta}} = \text{diag}(\mathbf{\Delta}, \mathbf{\Delta}_p). \end{aligned} \tag{7}$$

These relations are enabled by the Main Loop Theorem [33]. Robust stability is analyzed by performing a μ-analysis on the uncertain part of the closed-loop system $\mathbf{N}_{11}$ from $\mathbf{u}_\Delta$ to $\mathbf{y}_\Delta$ as indicated in the center in Fig. 5. To check nominal and robust performance, the uncertainty is augmented by a performance uncertainty $\mathbf{\Delta}_p$, closing the loop on exogenous inputs $\mathbf{w}$ and outputs $\mathbf{z}$, and evaluated for $\mathbf{N}_{22}$ and $\mathbf{N}$, as shown on the right in Fig. 5. While robust performance is originally defined as the condition $\|\mathbf{F}_u(\mathbf{N}, \mathbf{\Delta})\|_\infty \leq 1$ using the upper LFT introduced in Eq. 4, the Main Loop Theorem [33] allows to use the μ-relation as an upper bound on this condition, rendering the SSV a valuable tool.

The μ-synthesis algorithm finds a stabilizing controller that maximizes robust performance of the closed-loop system as given in Eq. 7 by alternating between H_∞-based controller design (K-step) and μ-analysis (D-step). If the condition for robust performance is fulfilled, the desired closed-loop performance targets are achieved even with the highest possible uncertainty present in the system. The SSV cannot be computed analytically, instead approximated upper (and lower) bounds using D-scales [34] are used, reading $\mu_{\tilde{\mathbf{\Delta}}}(\mathbf{N}(\mathbf{K})) < \min \bar{\sigma}(\mathbf{DN}(\mathbf{K})\mathbf{D}^{-1})$. This leads to the following setup of the μ-synthesis problem [9]:

$$
\begin{aligned}
&\text{Objective} && \min_{\mathbf{K}}(\min_{\mathbf{D}}\|\mathbf{DN}(\mathbf{K})\mathbf{D}^{-1}\|_\infty), \\
&D\text{-Step} && \text{find } \mathbf{D}(j\omega) \text{ as } && \min_{\mathbf{D}} \bar{\sigma}(\mathbf{DN}(\mathbf{K})\mathbf{D}^{-1})\ \forall\omega, && \text{such that } \mu_{\tilde{\mathbf{\Delta}}}(\mathbf{N}(\mathbf{K})) < \min \bar{\sigma}(\mathbf{DN}(\mathbf{K})\mathbf{D}^{-1}), \\
&K\text{-Step} && \text{find } \mathbf{K} \text{ as } && \min_{\mathbf{K}}(\|\mathbf{DN}(\mathbf{K})\mathbf{D}^{-1}\|_\infty), && \text{for fixed } \mathbf{D}.
\end{aligned}
\tag{8}
$$

Starting point for the synthesis is a control design K-step on the scaled plant $\mathbf{DND}^{-1}$ initialized with D-scales. The modeled uncertainties and their effect on the control commands are taken into account since the H_∞-norm is evaluated not only from exogenous inputs to outputs, but between $[\mathbf{u}_\Delta, \mathbf{w}]^T$ and $[\mathbf{y}_\Delta, \mathbf{z}]^T$ of the scaled plant $\mathbf{DND}^{-1}$. After each K-step, the frequency-dependent D-scales are adapted as the outcome of the robust-performance-based μ-analysis in the D-step. The D-scales are approximated by transfer functions of low order [34], in order to keep the order of the resulting controller as low as possible [10]. Scaling the plant alters the interaction between plant and uncertainties, informing the controller on how to minimize the effect of uncertainties. The D-K-iteration is performed until a satisfactory result is achieved, either by $\mu_{\tilde{\mathbf{\Delta}}} < 1$ or a H_∞-norm reaching the minimal achievable level γ_{min}.

B. Generalized Plant Formulation with Uncertainties

The introduced μ-synthesis method is implemented in the Robust Control Toolbox of MATLAB [35]. The challenge for the controller designer hence is the setup of the generalized plant $\mathbf{P}$ and the choice of its weighting functions and uncertainties resulting in the $\mathbf{P}$-$\mathbf{\Delta}$-structure. The following two subsections address this challenge, in order to bridge the gap between the above summarized theory of μ-synthesis and its practical applicability to the GLA problem.

To define a suitable generalized plant for the GLA problem, the control targets need to be defined:

1) reduce the integral loads at the wing root: wing-root bending moment (WRBM) and wing-root torsion moment (WRTM), the reduction of the WRBM is prioritized,
2) ensure stability of the closed loop system,
3) ensure robustness against uncertainties in the modeling, changing operating conditions and output disturbances due to sensor measurements,
4) work for the entire range of gust gradients defined as well as other atmospheric disturbances,
5) minimize the control activity and limit the bandwidth of the controller.

The above listed objectives can be grouped into performance, control activity, and robustness (stability) requirements. Hence, it is useful to define the generalized plant in a way that each of these requirements can be addressed by a weighting function. Ideally, the resulting generalized plant $\mathbf{P}$ or closed-loop system $\mathbf{N}$ would feature a transfer matrix with decoupled elements to address each of those requirements separately, however this is hardly achievable in practice. Figure 6 presents the generalized plant proposed to address the GLA problem.

The exogenous input $\mathbf{w}$ is the gust disturbance w^G. The GLA controller designed here only serves the purpose of disturbance rejection [9], thus no reference tracking input is provided. The first exogenous output $\mathbf{z}_1$ addresses the performance requirements. It is defined on the loads output $\mathbf{y}_{\text{load}}$, the WRBM and WRTM. These loads are an additional output that will not be used as a feedback variable (loads are not measurable), but prove to be beneficial to consider performance requirements when shaping the closed-loop transfer function. The loads output allows to directly assess

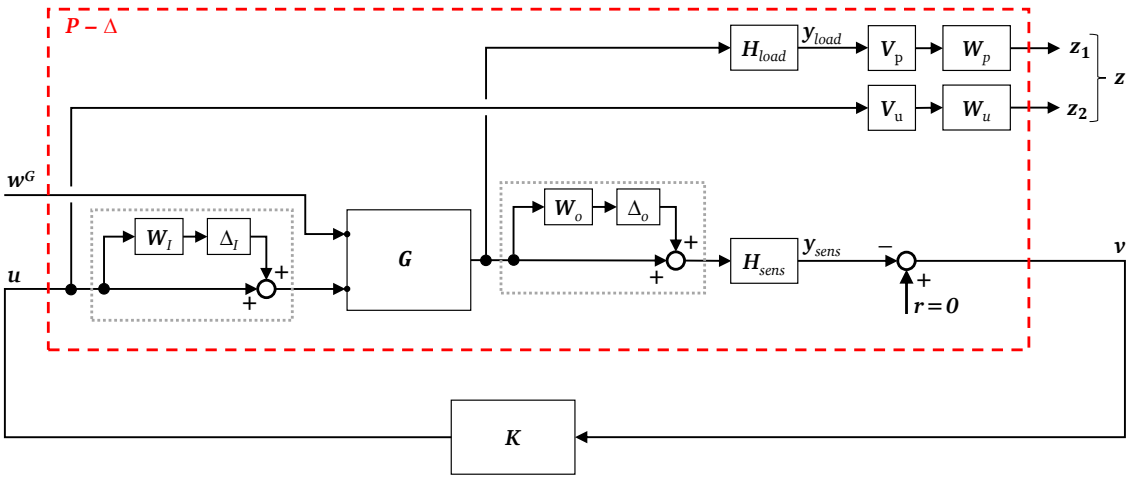

Fig. 6 Generalized plant for gust load alleviation control, with uncertainties for sensors and actuators.

the quantity that should be reduced and include it in the H_∞-norm that will be minimized. An alternative - however less intuitive - would be the penalization of the acceleration measurements $\mathbf{y}_{\text{sens}}$, which are feedback variables.

To treat the control activity requirements, the second exogenous output $\mathbf{z}_2$ is defined on the control commands vector $\mathbf{u}$. This is straightforward and directly allows to penalize control activity in certain frequency regimes.

The third requirement on robustness is usually treated by penalizing the feedback variables or errors, here labeled $\mathbf{v}$. This allows to access the sensitivity function of the closed-loop system, see [31]. In μ-synthesis however, an uncertain system is defined, and this uncertainty definition can be used to impose robustness and stability requirements. It is proposed to define uncertainties at the actuators and sensors, i.e. at plant inputs and outputs. This allows to independently access the stability at input and output, the typical cut-points to evaluate stability margins. Otherwise stability might be enforced only at one of those cut locations, while the other location sees small margins. Furthermore, this allows a very intuitive interpretation of the defined uncertainty: an actuator command for a flap deflection of a certain degree might not be matched perfectly, resulting in a slightly deviating flap position. On the output side, an acceleration measurement underlies a deviation due to measurement error, leading to slight differences compared to the actual acceleration.

As proposed by [34] and [36], a complex multiplicative structured uncertainty is applied to both the plant input and output, i.e. within actuators and sensors. "Complex uncertainty" refers to a uncertain plant parameter that is treated as a complex number, allowing for deviations in both the real and imaginary component. While this concept does not have a direct physical interpretation for the parameter itself, it can be viewed as representing simultaneous variations in gain and phase. Furthermore, complex uncertainties are preferred over real uncertainties, as they enable the formulation of the optimization problem using only D-scaling, rather than requiring both D- and G-scaling [37, 38]. "Structured uncertainty" means that the uncertainty matrices at the plant's input $\mathbf{\Delta}_I$ and output $\mathbf{\Delta}_o$ are diagonal, such that the uncertainty of one sensor or actuator does not interact with other elements. Otherwise, nonphysical interactions would occur, leading to increased robustness requirements. Finally, "multiplicative uncertainty" means that the following multiplication-structure is applied to define the uncertain plant $\tilde{\mathbf{G}}$ [9]:

$$\tilde{\mathbf{G}} = (\mathbf{I} + \mathbf{W}_o\mathbf{\Delta}_o) \cdot \mathbf{G} \cdot (\mathbf{I} + \mathbf{W}_I\mathbf{\Delta}_I), \qquad \text{with } \mathbf{\Delta_I} = \text{diag}(\delta_{Ii}) \text{ and } \mathbf{\Delta_o} = \text{diag}(\delta_{oi}). \tag{9}$$

The parameters of the aeroelastic model itself are considered to be certain, the uncertainty is captured within sensors and actuators. When individual parameters of the model are known to be uncertain, the uncertainty can be directly defined for those parameters. In primary flight control this could be the lift coefficient used in a six degree-of-freedom model [36]. For aeroservoelastic applications like GLA however, it is often easier to capture the uncertainty at the plant input and output, rather than trying to assign uncertainty individually to e.g. the stiffness or aerodynamic matrices.

The generalized plant as shown in Fig. 6 can be transferred into the typical $\mathbf{P}$-$\mathbf{\Delta}$-structure from Fig. 5. Applying the lower LFT from Eq. 4. yields the closed-loop system $\mathbf{N}(\mathbf{P}, \mathbf{K})$, whose transfer function will be shaped in μ-synthesis.

Typically, the plant $\mathbf{G}$ within the generalized plant $\mathbf{P}$ is normalized or scaled at it's inputs and outputs, see for example [9]. However, [31] proposes a separation of static and dynamic weights, eliminating the need for plant scaling and instead including such a scaling into the static weights. This approach is used here, leading to the definition of static weights $\mathbf{V}$ and dynamic weights $\mathbf{W}$ in Fig. 6. The weighting functions are chosen in the following subsection.

C. Weighting Functions for Performance, Control Activity, and Robustness

Having defined the setup of the generalized plant, the next step is to select the weighting functions used in the performance, control activity, and robustness channels. For active GLA, the focus of control action lies in the frequency regime of the first flexible eigenfrequency, in the coupled system (i.e. with the effect of aerodynamics) at about 9 Hz or 56 rad/s. The higher-order flexible eigenmodes have a significantly lower impact on the gust loads, i.e. it is sufficient to damp the first eigenmode for an effective GLA. Additionally, the actuators feature a roll-off frequency that does not allow to access eigenmodes beyond the first one (also refer to Table 1). As mentioned above, it is difficult to decouple the control objectives, i.e. there is some cross-coupling between the control objective channels. The weights presented in the following are the result of an iterative process to optimize the performance and robustness of the controller.

The performance channel directly penalizes the loads (WRBM, WRTM) induced by a gust, such that these loads are reduced by the controller. Another option would be a penalization of the modal velocity, as this directly relates to modal damping. However, it seems straightforward to include the quantity to be minimized within the H_∞-norm. As suggested by [31], the performance weight is divided into a dynamic weight $\mathbf{W}_\mathrm{p}$ and a static weight $\mathbf{V}_\mathrm{p}$. The frequency-dependent dynamic weight imposes a shape and is centered at 0 dB, while the static weight scales the performance output to achieve a certain magnitude in the output weighting.

Starting with the dynamic performance weight $\mathbf{W}_\mathrm{p}$: load alleviation shall be achieved in the frequency regime of the first aeroservoelastic eigenfrequency at about 9 Hz. In the high-frequency regime load reduction is not a target, which is why the performance weight should feature a roll-off there. The required steepness of the roll-off depends on the magnitude of the subsequent eigenmodes. In the low-frequency regime a wash-out would avoid an emphasis of performance towards the steady-state. However, the wind tunnel application of the GLA constitutes a special case: the wing will be clamped at the wind tunnel wall. In this scenario, even low frequency gusts (and even a steady-state gust, i.e. static angle of attack) affect the wing-root loads. In a free-flying aircraft, these low-frequency gusts would hardly be noticeable in the wing-root loads, as the aircraft responds by a rigid-body motion rather than flexible wing deformation, see e.g. [39]. Hence, it was found useful to not include a wash-out in the performance weight, but only slightly reduce the magnitude below the 0 dB line. The resulting weight can be seen in Fig. 7a.

The static performance weight $\mathbf{V}_\mathrm{p}$ combines the task of scaling the performance output of the plant and selecting the desired level of load alleviation. The normalization is performed by multiplying the plant output with the inverse of the H_∞-norm from exogenous input to the respective output, i.e. $1/\|\mathbf{G}_{\mathrm{w}\to\mathrm{z}_{1,\mathrm{i}}}\|_\infty$, with $i = 1, 2$ for WRBM and WRTM. In a singular value plot this results in the peak of the transfer function reaching the 0 dB line. To achieve a certain level of gust load reduction the weight is multiplied by the performance parameter p_red. The parameter selects how far the transfer function from exogenous inputs to performance outputs extends above the 0 dB line. Tuning this parameter serves as an intuitive option to require more or less performance. The result can be seen in 7b, showing the magnitude of the maximum singular value from $\mathbf{w}$ to $\mathbf{z}_1$. The combined weight $\mathbf{V}_\mathrm{p} \cdot \mathbf{W}_\mathrm{p}$ is presented in Fig. 7a.

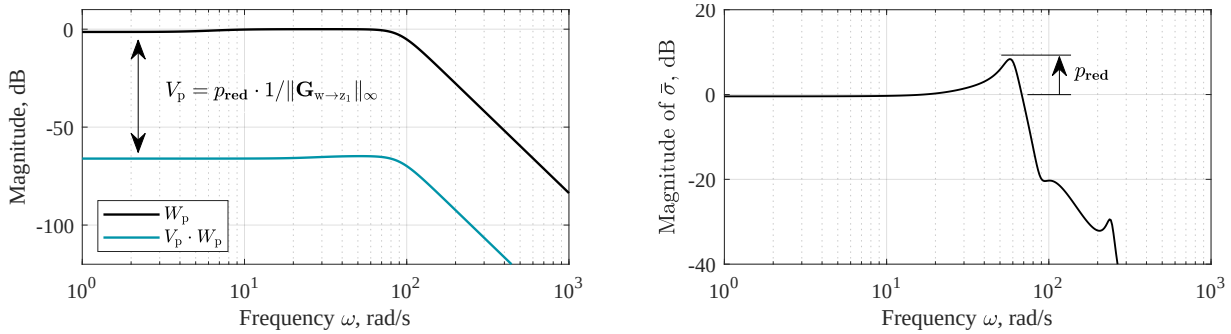

(a) Performance weighting functions $\mathbf{W}_\mathrm{p}$ and $\mathbf{V}_\mathrm{p}$. **(b) Max. singular value from input w to perf. output $\mathbf{z}_1$.**

Fig. 7 Performance weighting functions and resulting generalized plant singular value.

For the controller to be applied in the GLA wind tunnel experiment, the performance parameter p_red is chosen at a value of 2.5. This ensures that the transfer function lies on the 0 dB line in the low-frequency regime, while the entire peak associated with the first eigenmode extends above this line. As a result, nominal performance, as defined in Eq. 7, is achieved if the controller can limit the closed-loop loads around the first eigenfrequency to a level no higher than at low frequencies. For a free flying aircraft, the performance parameter would likely be chosen smaller, just enough to adequately damp the first eigenmode.

The performance channel weighting is also separated into a dynamic and static weight. The frequency-dependent weight $\mathbf{W}_\mathrm{u}$ has the shape of an inverted band-pass filter, with its minimum defined at 0 dB. The minimum is achieved at around 9 Hz or 56 rad/s, which is the frequency regime where loads shall be reduced, i.e. control activity enabled. To avoid control action in the high-frequency regime, the weighting function rises beyond the actuator cutoff frequency of approximately 90 rad/s. This avoids the amplification of noise and disturbances at high frequencies, and also avoids control commands that the actuators cannot achieve. Towards low frequencies the gain of the control activity weight also rises in order to avoid steady-state deflections of the control surfaces, as well as an undesired interaction of the GLA controller with a potential primary flight controller. The wash-out frequency depends on the location of the first flexible eigenfrequency in relation to the rigid-body eigenfrequencies, here 2.4 Hz or 15 rad/s were selected. The order of the wash-out and roll-off depends on the dynamics of the system, here an order of three was selected for the wash-out, while a first order roll-off proved to be sufficient. The resulting $\mathbf{W}_\mathrm{u}$ function is shown in Fig. 8a.

The static control activity weight $\mathbf{V}_\mathrm{u}$ shifts the dynamic weight to the adequate magnitude level. μ-synthesis will aim to push the H_∞-norm to 0 dB, to achieve nominal performance. Therefore, it makes sense to define the control activity weight in a way that 0 dB is reached when the deflection limit of the control surfaces is reached, see Table 1. This can be achieved by choosing $\mathbf{V}_\mathrm{u}$ as the inverse of the deflection limit, here 14°. This integrates a soft constraint on maximum flap deflection (a hard constraint is not realizable). To facilitate tuning, the parameter p_u is multiplied to the static weight. As for performance, this parameter is an intuitive tuning option to allow more or less control activity. The result of combining static and dynamic weight is also shown in Fig. 8a.

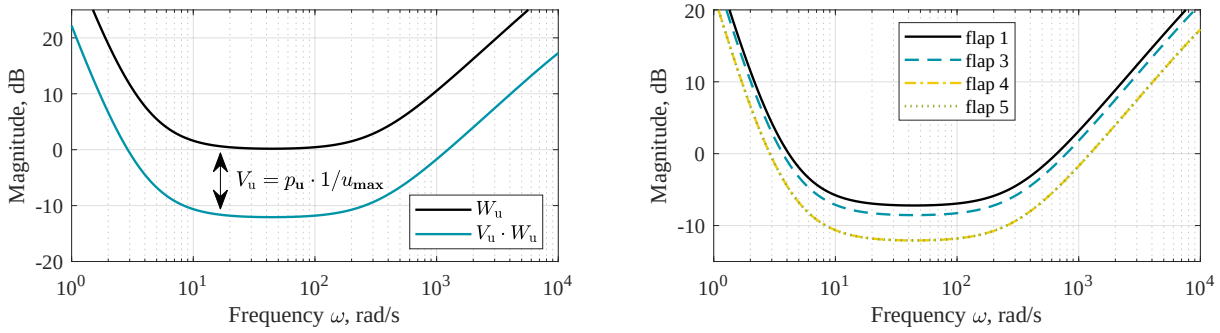

(a) Control activity weighting functions $\mathbf{W}_\mathrm{u}$ and $\mathbf{V}_\mathrm{u}$. **(b) Individual weighting of the control surfaces.**

Fig. 8 Control activity weighting functions and individual control surface weighting.

The control activity weight moreover allows to propose a weighting for the usage of the available control surfaces, see Fig. 3. Control surfaces can be penalized individually by adapting the parameter p_u for each control surface. The choice of such an individual weighting requires insight into the system to be controlled. Section II.B found flaps 4 and 5 most effective for addressing the wing-root loads in the frequency range of interest. The control activity weight takes this into account and penalizes these control surfaces less than flap 1 and 3. By increasing the gain for flap 3 by 50% and for flap 1 by 75%, the preferred usage of the control surfaces is indicated to the controller. The resulting weights are shown in Fig. 8b. Sections IV and V will evaluate the implications of the individual weighting.

The advantage of μ-synthesis compared to pure H_∞-based loop shaping is the possibility to define uncertainties and achieve robust performance under these uncertainties. Therefore, it makes sense to choose the uncertainty weighting functions at actuators and sensors reasonably, based on physical insight about the actuator and sensor properties. μ-synthesis will then try to achieve robust stability and performance (Eq. 7) under these uncertainties. Other than in H_∞-based loop shaping, the weighting functions defined for the uncertainties do not directly shape a transfer function such as the sensitivity function (see for example [31]), but implicitly yield certain stability margins. If the stability margins are found to be insufficient, the uncertainties can be increased to achieve a better behavior. Uncertainties can thus be used as a tool to achieve the desired stability properties, while ensuring that the controller remains effective even if the real system deviates from the model.

Inspired by [36], the actuator uncertainty is 5% at low frequency and 10% at high frequency, with a crossover frequency of half the actuator roll-off, i.e. approximately 45 rad/s. The resulting weighting function is shown in Fig. 9a. How this affects the actuator magnitude is shown in Fig. 9b, depicting the multiplicative uncertainty term $(\mathbf{I} + \mathbf{W}_\mathrm{I}\mathbf{\Delta}_\mathrm{I})$ from Eq. 9. The nominal value of the uncertainty is one, or 0 dB. The family of functions resulting due to the uncertainty

is governed by the robustness weight, hence the possible deviation from the nominal value increases over frequency. All actuators receive the same uncertainty weight, as the actuators are of the same type. A weighting of the used control surfaces is already implemented within the control activity weight.

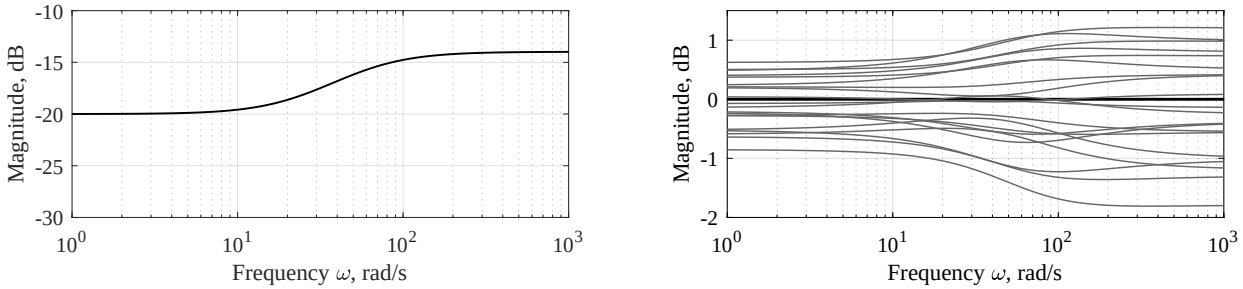

(a) Robustness weight for each actuator W_I. **(b) Multiplicative uncertainty in the actuator magnitude.**

Fig. 9 Actuator uncertainty weight and the resulting actuator uncertainty.

As mentioned above, uncertainties should be defined at the plant input and output, in order to achieve satisfactory stability margins at both cut locations. The uncertainty weight for the sensors is shown in Fig. 10a. Similar to the actuator robustness weight, the uncertainty rises towards higher frequencies, with the crossover frequency now being 90 rad/s. A smaller level of uncertainty is defined compared to the actuators, because the sensor measurements are more precise than actuator positions. 2.5% and 5% uncertainty are selected at low and high frequencies, respectively.

The sensor uncertainty weight allows to force a preference for the usage of available sensors (Fig. 3). Similar as for the control activity weight, system insight is required for a reasonable choice. For GLA a weighing of the sensors based on their location and the resulting signal-to-noise ratio is proposed. The sensors located further inboard do not capture the first wing bending as effectively as the further outboard located sensors, since the acceleration is greatest near the wing tip. Therefore, the uncertainty level is amplified by a static gain of one for the outboard sensors 5a/b, a gain of 2.5 for sensors 4a/b, a gain of 4.0 for sensors 3a/b, and a gain of 5.0 for sensors 2a/b. Note that the innermost sensors 1a/b were not used by the GLA controller. The effect of the uncertainty on the output of the sensors when the plant is excited by a gust is presented in Fig. 10b. It becomes clear that the uncertainty band increases for further inboard sensors, and it also increases towards high frequencies for all sensors.

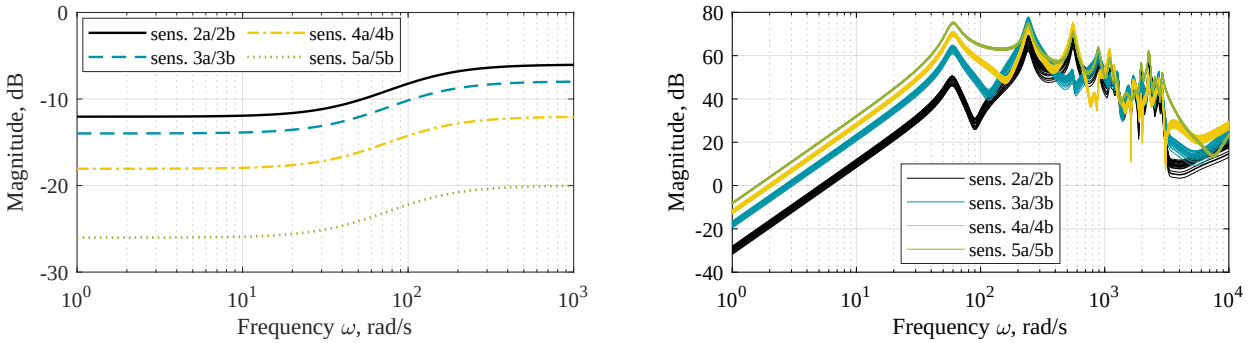

(a) Robustness weights for the sensors W_o. **(b) Uncertain plant dynamics.**

Fig. 10 Sensor uncertainty weight and the resulting uncertain plant output.

With the above selected weighting functions the setup of the μ-synthesis problem for the GLA controller is complete, and is handed to the algorithm sketched in Eq. 8. An important advantage of specifying the control targets within top-level weighting functions and uncertainties, is that the controller configuration can be adapted without the need for changes in the top-level setup. The following section will explore different controller configurations, with a different set of sensors and actuators, all synthesized with the same weightings and uncertainties as presented above.

IV. Simulation-Based Assessment of the GLA Controllers

Using the developed generalized plant, along with its weighting function and uncertainty models, the gust load alleviation controller for the wind tunnel experiment is synthesized using the μ-synthesis algorithm given in Eq. 8. As outlined in the introduction and detailed in the previous section, a benefit of robust control is the abstraction of the control problem into a higher-level formulation, rather than directly tuning controller gains. This approach makes the design process adaptable to varying configurations of feedback sensors and control surfaces. Additional sensors and control surfaces, provided they have the same properties as the initial ones, can be incorporated into the controller, without requiring any adjustments to the synthesis setup presented in Section III. This section demonstrates this flexibility by evaluating three different controller variants, each using a distinct subset of control surfaces and acceleration sensors (see Fig. 3 for the location of the listed sensors and surfaces). Table 2 lists the controller variants.

Table 2 Controller variants with different control surfaces and sensors.

ID	Controller name	Flaps in use	Sensors in use	Remark
1	Baseline	4, 5	5a, 5b	-
2	Added Sensors	4, 5	2a, 3a, 3b, 4b, 5a, 5b	sensors 1a, 1b ineffective; sensors 2b, 4a inoperative
3	Added Actuators	1, 3, 4, 5	5a, 5b	flap 2 inoperative

For controller synthesis, it is beneficial to use a reduced order model of the plant $\mathbf{G}$, since the order of the controller equals the order of the plant in unstructured μ-synthesis [9]. Additionally, computational effort is reduced. Standard reduction techniques such as balanced truncation [40] are available in MATLAB. The weighting functions from Section III led to the results presented in this section. During the iterative tuning process it was found that the control activity weight should be lowered in order to improve the performance of the controller, such that the parameter $\mathbf{p}_u$ (see Fig. 8) was changed from initially 1 to 0.25. All other weighting functions remained unchanged.

Controller design is carried out at a freestream velocity of 50 m/s and a corresponding Mach number of 0.15 under ambient atmospheric conditions. However, this section focuses on the evaluation at a freestream velocity of 30 m/s, in line with the experimental results presented in Section V. This condition was where the controllers were tested most extensively. It is observed that the controller can be scaled to any of the three freestream velocities (30, 40, and 50 m/s) tested in the wind tunnel by applying a simple gain scheduling based on dynamic pressure. This straightforward scaling is feasible because the linear aerodynamic matrices scale with dynamic pressure, and the eigenmode dynamics change by only 0.5 Hz across the tested speeds. Since the results at different velocities are similar, they are not discussed in detail in this paper, except for a comparison at the end of Section V.

This section will analyze the controllers regarding performance, control activity, and robustness. The assessment is performed within the linear simulation environment introduced in Section II. The full order linear state-space model is used for the analysis, including the feedback loop time delay of 8 ms (6 ms from the actuators, and 1 ms each from sensors and controller processing, see Table 1). The reduced order model (also including the 8 ms time delay) is used only for the controller synthesis process. A nonlinear validation of the controllers in a simulation environment was also performed prior to entering the wind tunnel. The results will not be presented here, since they are very similar to the experimental data. Linear models allow a frequency domain evaluation of the controllers, and tools like disk-based stability margins [41] as well as μ-analysis [32] can be applied.

A. Performance Evaluation

All three controllers are designed for the same control objectives, using the same generalized plant, uncertainties, and weighting functions as developed in Section III. Therefore, the achievable performance of all controllers shall be the same. Performance is evaluated in Fig. 11, depicting the transfer function between a gust input w^G and the wing-root bending moment. The same frequency behavior can be observed in the maximum singular value plot from exogenous inputs to exogenous performance outputs in a generalized plant with no weighting functions.

Figure 11a compares the open and closed loop frequency response for the baseline controller, using the two sensors near the wing tip (5a, 5b), and the two outer control surfaces (4, 5). These control surfaces match the outer ailerons on a current transport aircraft best. In the figure, the peak caused by the first aeroelastic mode at about 9 Hz or 56 rad/s is clearly visible. The controller is able to greatly reduce the bending moment in this frequency regime. At 56 rad/s the reduction is 14 dB, or a relative reduction of about 80% with respect to the open loop case. Time domain results will be presented for the experimental evaluation in Section V, showing similar levels of load reduction. For other frequencies

the reduction is lower, almost disappearing between open and closed-loop system in the frequency regime below 2 and above 150 rad/s. This is due to the imposed performance and control activity weight presented in Section III.

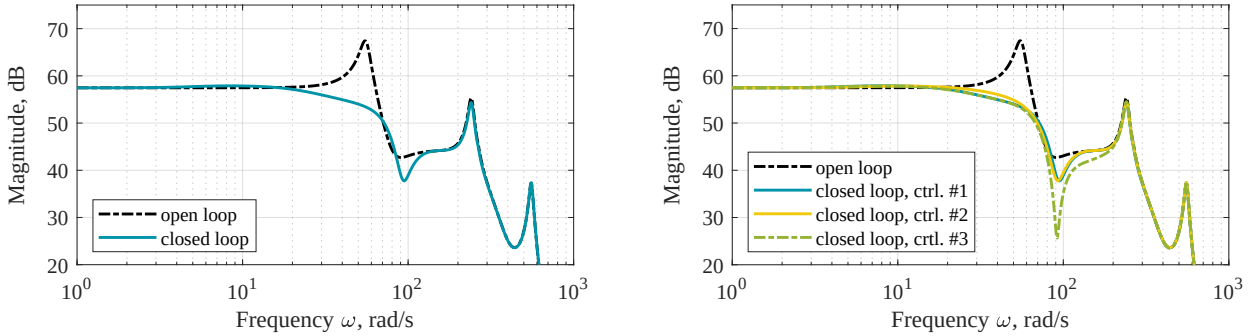

(a) Baseline Controller (ID 1). **(b) Controller comparison (IDs 1, 2, 3).**

Fig. 11 Performance evaluation: transfer function from gust w^G to WRBM, open and closed loop.

Figure 11b shows the performance evaluation for the three controllers (see Table 2) in comparison. As expected, all controllers feature a very similar closed loop frequency response. This confirms that the same top-level μ-synthesis setup leads to the same results with respect to the transfer functions from exogenous inputs to exogenous performance outputs. However, the inner structure of the controllers are different, as the following subsections will show.

B. Comparison of the Control Surface Setup

Load reduction is achieved by deflecting the control surfaces, thereby adding camber to the wing, altering the lift, and hence the wing-root loads. Figure 12a evaluates the control activity of the baseline controller, with $u_{\mathrm{x,cmd,i}}$ denoting the command send to flap i. The focus of the controller is to reduce the amplification of loads in the regime of the first aeroelastic eigenfrequency, leading to a damping of this eigenmode. Therefore, the control activity is highest around the 9 Hz or 56 rad/s. Wash-out towards low frequencies and roll-off towards high frequencies is successfully integrated in the controller transfer function, thereby avoiding steady-state interaction, too fast or too slow control commands, and adverse effects of sensor bias and noise. This is mandated by the control activity weight from Section III.C. As anticipated based on the results in Section II.B regarding control surface effectiveness, the controller similarly utilizes flaps 4 and 5, given their comparable effectiveness in alleviating the wing-root loads.

It should be noted that μ-synthesis offers no possibility to strictly adhere to actuator or control surface limitations. Instead, these limits are soft requirements within the control activity weight. Hence, it is important to check that these limits are not exceeded in the controller design. This is best checked in the time domain, as will be done in Section V.

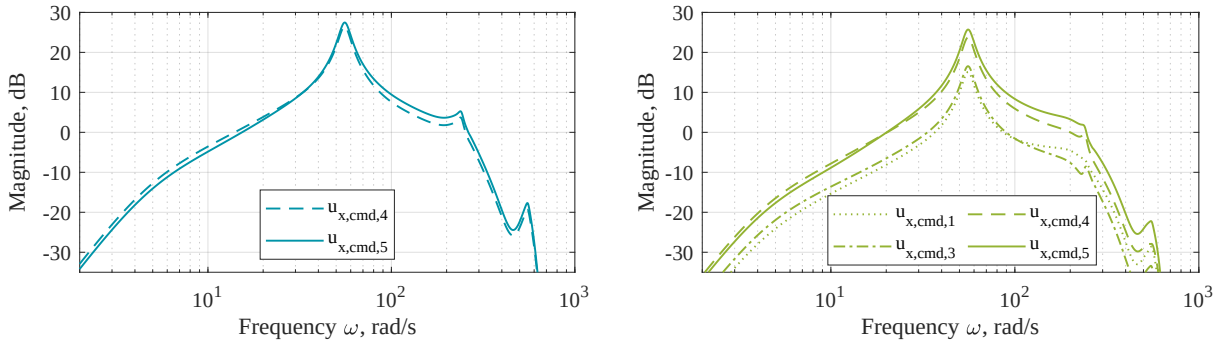

(a) Baseline Controller (ID 1). **(b) Added Actuators Controller (ID 3).**

Fig. 12 Controller comparison: Transfer function from gust w^G to control surface commands.

The added actuator controller (ID 3) uses the same sensors as the baseline controller (ID 1), but additionally adds flap one and three to the available control effectors. Both controllers lead to the same load reduction, as seen in Fig. 11, but the control surfaces are used differently. This is seen by comparing Fig. 12a and 12b. Since more control surfaces

are used by controller 3, the individual control surfaces have to deflect less. The peak for flap 5 reduces from 27.5 dB (controller 1) to 25.7 dB (controller 3), yielding a relative reduction of about 18%. In controller 3, as imposed by the different weighting of the control surfaces (see Fig. 8b), the outer flaps 4 and 5 are used the most, while the more inboard flaps exhibit a lower magnitude. This shows how the weights can be used to incorporate constraints within the controller design. If all control surfaces where used to their full extent, a higher performance could be achieved. This would however necessitate an adaption of the weighting function used in the controller synthesis. The setup used here demonstrates that the same performance can be achieved with less stress on the individual control surface.

C. Comparison of the Sensor Setup

Controller 2, or added sensors controller, uses the same control surfaces as the baseline controller, but receives additional information from the acceleration sensors 2a, 3a, 3b, and 4b. The inboard sensors 1a/b were not used as the signal-to-noise ratio was low. Sensors 2b and 4a produced incoherent experimental data, which is why these sensors were excluded. The different uncertainty weighting of the individual sensors, shown in Fig. 10, is now being applied.

Again, similar performance is achieved when comparing controller 1 and 2, see Fig. 11. Differences appear when comparing the controller transfer function from the sensors to the flaps. Figure 13a shows the baseline controller action from sensor 5b to flap 4 and 5a to flap 5, the remaining two transfer functions being very similar in their shape. Figure 13b shows the added sensors controller action from all used sensors to the fifth control surface.

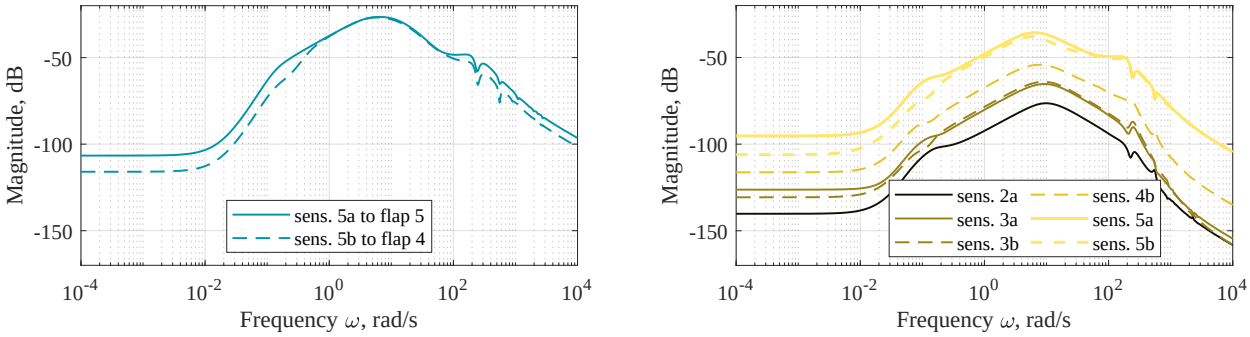

(a) Baseline Controller (ID 1), sensors 5a/b to flap 4/5. **(b) Added Sensors Controller (ID 2), all sensors to flap 5.**

Fig. 13 Controller comparison: Transfer function between sensors and control surface commands.

When more sensors are used, the magnitude of each individual sensor decreases. Furthermore, it can be seen that the sensor uncertainty weighting introduced in Fig. 10 is reflected in the usage of the sensors by the controller. The outboard sensors 5a/b with the best signal-to-noise ratio are used more than the further inboard ones. The difference in sensor usage follows the imposed weights. This demonstrates the utility of uncertainties for incorporating system knowledge in the controller design. Sensor usage is optimized based on the sensor characteristics.

The advantage of the added sensors controller is not performance, but the fact that acceleration information is obtained from more sensors, making the designed closed-loop system more robust in case of measurement error or sensor fault. As shown by the lower magnitude, the controller relies less on the two outboard sensors.

D. Stability and Robustness Evaluation

The controllers are also evaluated for stability and robustness, which is imposed by the actuator and sensor uncertainties as described in Section III. The stability assessment can be performed by evaluating disk-based stability margins [41] in magnitude and phase at the input and output. Results are shown in Table 3.

The multiloop stability margins of all three controller variants are similar. With a time delay of 8 ms in the linear full-order state-space system, the multiloop phase margin of the closed loop system is about 40°, while the multiloop gain margin is about 2 in absolute values, meaning 6 dB. These margins are found both at the input and the output of the plant. This indicates a balanced design, where no performance remains unused. The margins are considered sufficient. Multiloop margins are rather conservative, assuming disturbances in all channels simultaneously [41]. Loop-at-a-time margins are less conservative, and yield a margin of 3.4 (10.7 dB) in gain and 57° in phase for the baseline controller, again almost similar at input and output. Loop-at-a-time margins for the other two controllers are similar and therefore not presented in the table.

Table 3 Disk-based stability margins for all three controllers.

ID	Controller	Margin type	Cut point	Gain margin	Phase margin	Frequency
1	Baseline	multiloop	input	2.2 (6.8 dB)	40.7°	14.8 Hz
		multiloop	output	2.2 (6.8 dB)	40.6°	14.9 Hz
		loop-at-a-time	input	3.4 (10.7 dB)	57.5°	15.9 Hz
		loop-at-a-time	output	3.6 (11.0 dB)	58.6°	15.4 Hz
2	Added Sensors	multiloop	input	2.4 (7.6 dB)	45.0°	15.1 Hz
		multiloop	output	2.4 (7.6 dB)	45.0°	15.3 Hz
3	Added Actuators	multiloop	input	2.2 (6.7 dB)	40.4°	14.8 Hz
		multiloop	output	2.3 (7.2 dB)	42.7°	14.8 Hz

Due to the specifications of uncertainties in the system, robustness can be evaluated by applying a μ-analysis [32]. Robust stability, nominal performance, and robust performance can be evaluated as introduced in Eq. 7. The result for the baseline controller is displayed in Fig. 14 below. Similar results are achieved for the other controller variants, and therefore omitted here. It should be noted that this evaluation is always linked to the definition of uncertainty, here at the plant input (actuators) and output (sensors), as displayed in Fig. 9 and Fig. 10, respectively.

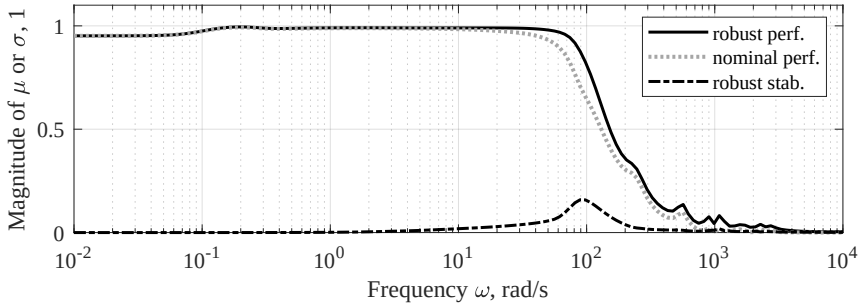

Fig. 14 Results of the μ-analysis for the baseline controller (ID 1).

Robust stability reaches a peak of about 0.15. This indicates that all uncertainties defined on the sensors and actuators can be increased by a factor of 6.7 (1 divided by 0.15) before the system becomes unstable [9]. This can be checked by extracting the worst-case $\mathbf{\Delta}$ matrix [36], i.e. the smallest uncertainty matrix that would render the system unstable, see Eq. 6. For the baseline controller it is a four-by-four diagonal matrix, one for each uncertainty, with values of about 6.8, matching the results depicted in Fig. 14.

Nominal and robust performance μ-values do not differ much. A difference emerges only if uncertainties become relevant for stability. This is the case around the first aeroelastic eigenfrequency of 56 rad/s. Nominal and robust performance reach a maximum value of 0.99, just below 1. This indicates that the controller is able to achieve a performance almost exactly as high as the one mandated by the performance weight, also under the defined uncertainties. Since the performance weight was chosen to exceed the 0 dB line by the value of p_{red} (see Fig. 7), the controller is able to push the peak of the closed loop system just below the 0 dB line. At the same time, the control activity does not lead to a level above 0 dB either. The result of the μ-analysis is in accordance with the performance shown in Fig. 11, i.e. a reduction of the wing-root loads around the eigenfrequency to a level not higher than in the low frequency regime.

V. Experimental Assessment of the GLA Controllers in the Wind Tunnel

In a final step, the developed controllers are assessed in the wind tunnel experiment, which is shown in Fig. 1. Details on the flexible wing used in the test are given in [13]. The gust generator can create both continuous periodic gusts (sine-like) and discrete gusts (1-cos-like). The gust profiles are not as clean as in a simulation, since the primary gust frequency is superimposed with higher harmonic frequencies. The slotted cylinders of the gust generator lead to a frequency pattern in which integer multiplies of the turning frequency are pronounced. Additionally, random disturbances occur in the airflow. More information on the gust generator can be found in [14].

The flexible wing model is mounted on a balance, which measures the forces and moments at the wing root. A real-time control system (Jaeger System) executes the controller at a sample frequency of 1000 Hz. The controller is fed with the signals from the acceleration sensors, and outputs control commands. These commands are converted to duty cycles and fed to the electromechanical actuators, which execute the commands at 560 Hz. A Dewetron system is used to record all measurement data, operating at 3000 to 10000 Hz. An Image Pattern Correlation Technique (IPCT) [42] is used to track the motion of the flexible wing and the control surfaces.

In the following sections the different controllers introduced in Section IV are assessed based on the experimental data obtained in the wind tunnel test. The baseline controller with two control surfaces and two sensors is analyzed first, and in the subsequent sections compared to the other controller variants. The evaluation is performed at a freestream velocity of 30 m/s, the other speeds are detailed in Subsection V.C. The wing is tested at 0° angle of attack.

A. Baseline Controller (ID 1)

First, the controller's action during continuous gusts will be examined. These gusts are - as mentioned above - not ideally sinusoidal, but contain a larger frequency spectrum. To ensure comparability, the gust generator is kept running for 40 s at a certain continuous rotation frequency, while the controller is active from about 12.5 to 27.5 s. The controller is gradually switched on, increasing the gain at the controller output from zero to one. As expected from the simulations shown in Section IV, the effect in load reduction is most prominent at the first flexible frequency of about 9 Hz. The result for this frequency is shown in Fig. 15. At this frequency and speed, a gust angle of about 1.8° is induced.

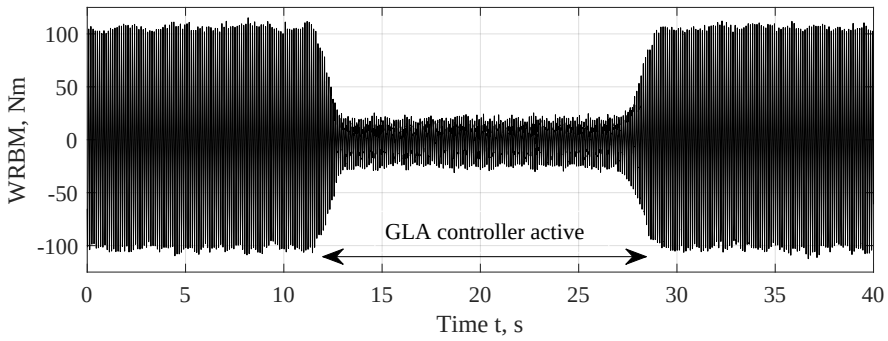

Fig. 15 Baseline controller: WRBM during a continuous gust excitation with 9 Hz.

The experimental data proves that the robust GLA controller drastically reduced the bending moment at the wing-root. In Fig. 15 the signal is mean-corrected, only considering the offset around the trim condition. The root mean square (RMS) value without controller is 72 Nm, while it drops to 14 Nm when the controller is turned on. A relative reduction of 80% can be achieved, in accordance with the simulation results. When the static WRBM of 50 Nm that is present at 0° angle of attack is taken as a reference (see [16] for further details), the relative RMS reduction is about 47%. It shall be mentioned once again that this is the best case, since the controller is specifically tuned to address this frequency regime, and a continuous gust allows more reduction than a discrete gust (see further below). Nonetheless, the controller also performs good in other frequency regimes, as will be shown. From a loads perspective, reducing the highest occurring load is the target, and the controller successfully addresses this objective.

Figure 16 shows the comparison of wing-root loads with and without active GLA for a one second excerpt in time. The wing-root bending moment is shown at the left, the torsional moment at the right. The WRBM plot re-states the results seen in Fig. 15, with a significant reduction in the RMS moment. The torsional moment is reduced as well, here the RMS reduction is from 44 to 8 Nm, yielding a 80% decrease. When taking the static WRTM level of -30 Nm at 0° angle of attack as a reference, the relative reduction is 48%. The backwards sweep of the wing and the resulting bending-torsion coupling is beneficial for reducing bending and torsional moments at the same time.

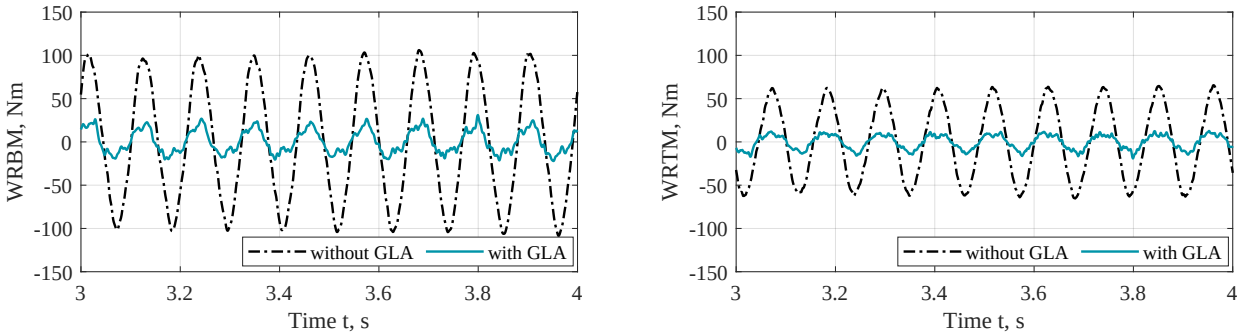

(a) Wing-root bending moment. **(b) Wing-root torsion moment.**

Fig. 16 Baseline controller: loads during a 9 Hz continuous gust, with and without GLA.

Load alleviation is achieved by deflecting the control surfaces in the same direction as the wing's motion imposed by the gust, thereby altering the wing's camber and increasing or decreasing the lift, which in turn reduces the loads at the wing-root. Figure 17 shows the commanded ($u_{\mathrm{x_cmd,i}}$, blue) and actual ($u_{\mathrm{x,i}}$, red) control surface deflection during the 9 Hz continuous periodic gust encounter. The commands are measured as an output of the hardware system executing the controller, while the actual control surface deflection is obtained by an Image Pattern Correlation Technique (IPCT). The lower side and the flaps of the wind tunnel model are equipped with optical markers, such that the motion of the wing and the flaps can be tracked and evaluated in post-processing. Further details on the method are given in [42]. It can be seen that the actual flap deflection closely follows the control commands, with a certain delay. The delay stems from the actuators, as found during the model identification presented in Section II.B. Since the commands do not exceed the deflection limit of 14° (see Table 1), the flap can respond to the commands in full.

As the effectiveness study in Section II.B and the frequency domain analysis in Section IV.B imply, the fourth and fifth control surface are utilized similarly. The pattern of the control surface commands indicates that the gust is not purely sinusoidal, but rather a superposition of multiple harmonic excitations.

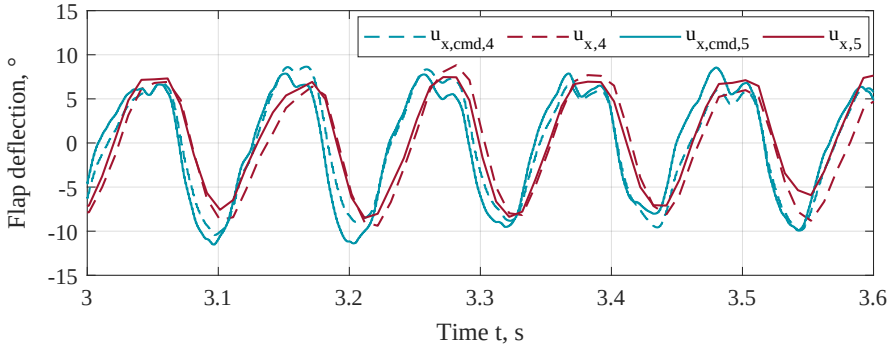

Fig. 17 Baseline controller: flap commands and position (from IPCT) during a 9 Hz cont. gust.

One control objective defined in Section III is that the GLA works for the entire range of relevant gust gradients. To evaluate the performance of the controller for other gust gradients than the one at 9 Hz, the gusts generator is set to numerous frequencies and the measurement procedure is repeated. The result is shown in Fig. 18. The crosses in black indicate the standard deviation in WRBM without controller for a specific gust frequency, while the blue crosses indicate the one with active controller. The biggest effect in load alleviation is undoubtedly seen at 9 Hz, but the experimental data suggests that the controller works for a range of gust frequencies. Additionally, the gust signal measured by the five-hole probe in the wind tunnel (see Fig. 1) is fed into the numerical simulation model, obtaining the bending moment to compare with experimental data. These are the black and blue dashed curves in the figure. A good match between simulation and experiment is observed. The simulation over-predicts the loads without controller in the lower frequency regime, while being close to the experimental data in the higher frequency regime. The load reduction achievable by the active GLA is slightly under-predicted by the simulation.

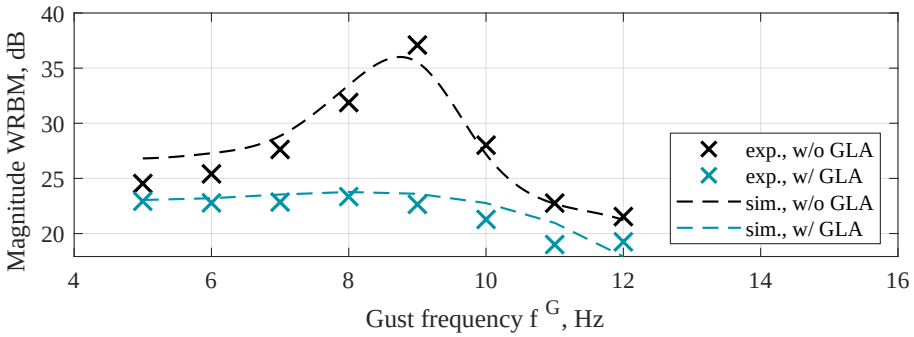

Fig. 18 Baseline controller: magnitude of WRBM with and without GLA at multiple frequencies.

Continuous periodic gusts are a rather academic scenario beneficial to evaluate the controller performance at distinct frequencies. A more realistic scenario is the interaction with discrete gusts, somewhat similar to the 1-cos gusts specified in the certification documents [29]. Discrete gusts are generated in the wind tunnel experiment by rotating the gust generator once, for example by 180°. The resulting loads with and without active GLA at a 9 Hz gust (pseudo) frequency are shown in Fig. 19a, the according control commands are shown in Fig. 19b. The baseline controller is able to significantly reduce the bending moment at the wing-root in the discrete gust case. The relative reduction of the load peak is 60%, from approximately 40 Nm to 16 Nm. This reduction is lower than in the continuous case, as frequencies other than 9 Hz are also excited in the discrete gust case. Moreover, the load magnitude is lower in general. The load reduction is achieved by a control surface deflection not larger than 7°, as seen in Fig. 19b. Disturbances and turbulence in the flow cause the control surfaces to show activity after the interaction with the discrete gust.

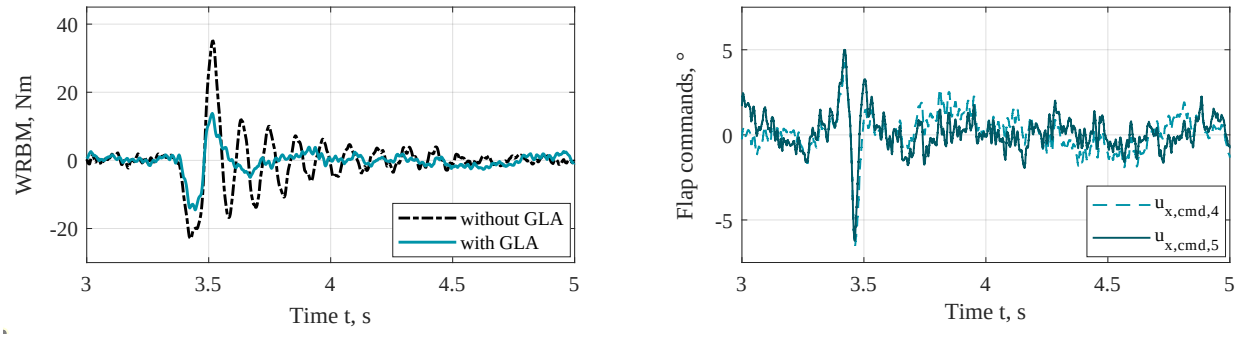

(a) Wing-root bending moment.

(b) Control surface commands.

Fig. 19 Baseline controller: WRBM and control commands during a 9 Hz discrete gust.

B. Added Sensors (ID 2) and Added Actuators (ID 3) Controller

Having evaluated the baseline controller in the experiment, the performance shall be compared to the other two controllers designed. The comparison for the added sensors controller is presented in Fig. 20. The left plot compares the reduction in WRBM during a continuous periodic gust of 9 Hz, the right plot shows the related control commands. As expected from the simulation assessment in the frequency domain (Section IV), the achieved load reduction of the added sensors controller closely matches the one of the baseline controller. Since the same control surfaces are available, the same holds for the controller commands of flap 4 and 5. The difference is the usage of the acceleration sensors, as described in Section IV.C. The experimental results confirm the findings in the simulation.

The added actuators controller is compared to the baseline controller in Fig. 21. The same comparison as for the added sensors controller is performed. The left plot confirms again that the reduction in bending moment at the wing-root is similar for both controllers. The difference of the added actuators controller compared to the baseline controller becomes visible in the right plot: the control surfaces used to achieve the load alleviation. With the inner control surfaces contributing to the load reduction, the outer control surfaces 4 and 5 are deflected less than in the baseline controller. This can be observed especially for the third to fifth peak. As found in the simulation evaluation

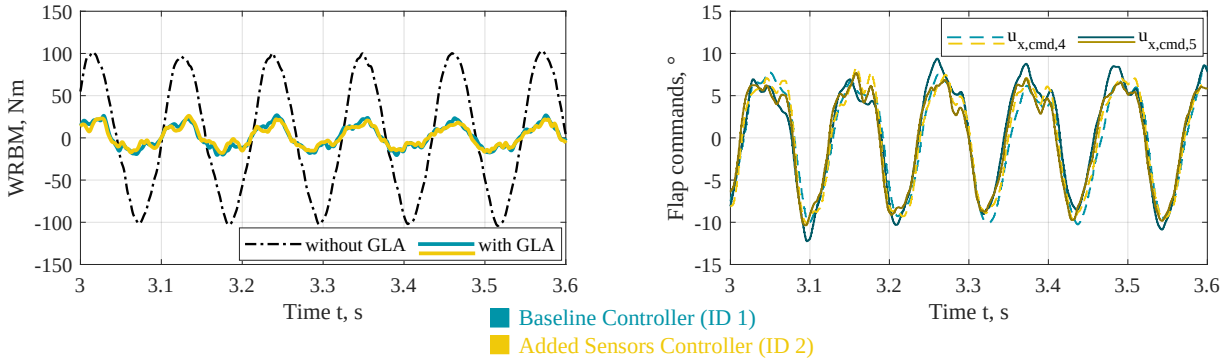

Fig. 20 Baseline vs. Added Sensors Controller: WRBM (left) and control commands (right).

in Section IV.B, the usage of the control surfaces is imposed by the weighting function for control activity. Flaps 1 and 3 are used less than flaps 4 and 5. If a greater load reduction is the target, the additional available control surfaces could be used in their full potential. This however would then necessitate a re-selection of the performance weighting function, as this implies a higher weighting of performance with respect to control activity. Here, it is shown that the same level of load reduction can be achieved with more flaps, reducing the stress on the individual control surface.

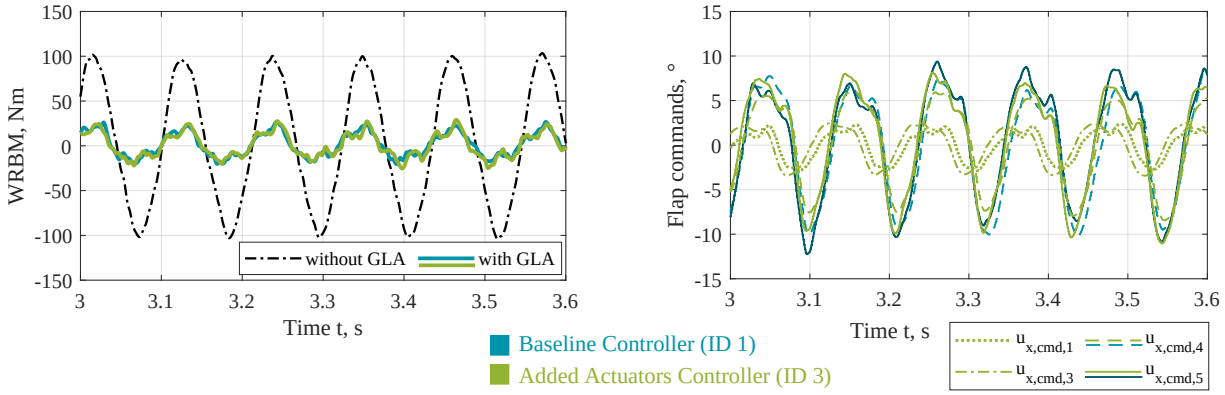

Fig. 21 Baseline vs. Added Actuators Controller: WRBM (left) and control commands (right).

Assessing the behavior of the controllers at other frequencies than 9 Hz, as done for the baseline controller in Fig. 18, is done for all three controllers in Fig. 22. Experimental results for the baseline, added sensors, and added actuators controller are compared in the frequency range from 3 to 12 Hz. Note that the experimental data are generated by rotating the gust generator at the respective frequency, and this is not a frequency response function per se.

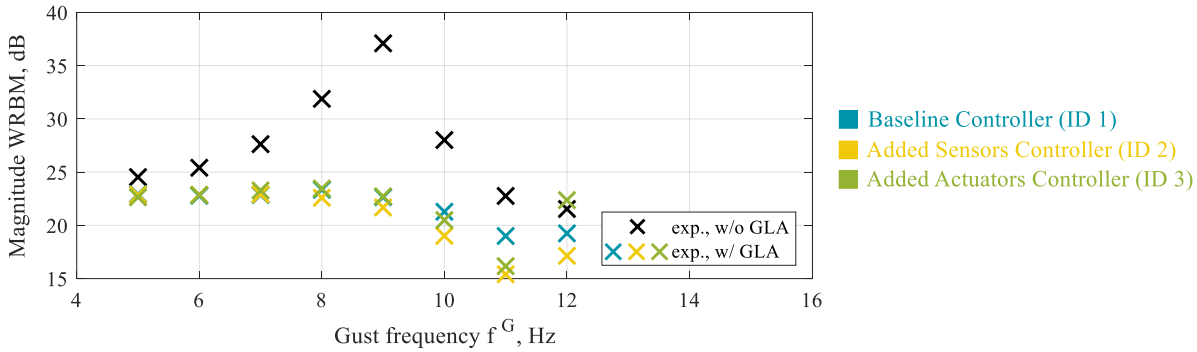

Fig. 22 Baseline vs. Added Sensors vs. Added Actuators Controller: WRBM at multiple frequencies.

Figure 22 confirms that the performance of the three controllers is similar for almost all gust frequencies, with deviations emerging only at 11 and 12 Hz. This result supports the previous finding that the same gust load alleviation potential can be achieved with different controllers, while the used sensors and control surfaces are altered.

C. Gain Scheduling for Adaptation to the Freestream Velocity

All experimental results presented above are obtained at a freestream velocity of 30 m/s, as the wind tunnel testing was conducted most extensively for this test condition. However, as discussed in Section IV, the controller is designed at a freestream velocity of 50 m/s, and then gain scheduled to perform at other operating conditions. Figure 23 evaluates the performance of the baseline controller at multiple freestream velocities within the wind tunnel.

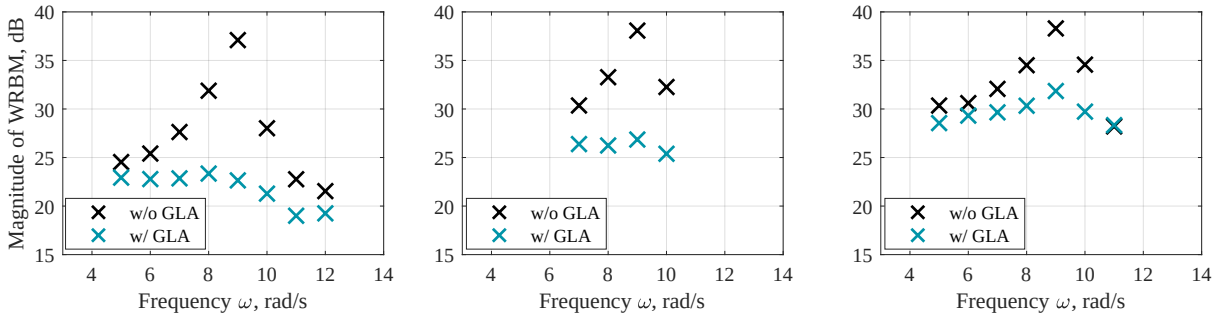

(a) Freestream velocity 30 m/s. **(b) Freestream velocity 40 m/s.** **(c) Freestream velocity 50 m/s.**

Fig. 23 WRBM due to continuous gusts at different frequencies, at multiple freestream velocities.

It is confirmed that the controller operates well at all investigated freestream velocities, also achieving similar stability margins. The load reduction seems to be best at 30 m/s, but a substantial load reduction is achieved for every speed, especially for a gust frequency of 9 Hz. At 40 m/s not all frequency points were tested. An evaluation for the added sensors and added actuator controller yields similar results to the baseline controller shown above. This final evaluation confirms the satisfactory performance of the gust load alleviation controllers designed using μ-synthesis.

VI. Summary and Outlook

This paper presents the application of μ-synthesis robust control to design a gust load alleviation controller for a flexible wing tested in a wind tunnel experiment. An overview of the aeroservoelastic modeling procedure, model identification, and model update is given, in order to obtain a numerical representation of the wind tunnel experiment for controller design and validation. The robust control design method μ-synthesis is introduced. Emphasis of the paper is to bridge the gap between the mathematical foundation of the method and its practical applicability. Detailed information on the proposed definition of the generalized plant for the GLA problem is provided, including the selection of performance, control activity, and uncertainty weights. The proposed synthesis setup can serve as a guideline for application to similar aeroservoelastic problems. It is shown how to incorporate system knowledge within the controller design, leading to an optimized usage of available sensors and control effectors. Applying the same top-level weighting functions, three controllers using different sets of control surfaces and feedback sensors are designed. The controllers are first evaluated in the simulation environment, before being experimentally validated in the wind tunnel test. All controllers show a satisfactory performance and robustness. Experimental results suggest the gust loads can be reduced by up to 80%, when referring to the deviation from the trim point. This reduction was obtained for a continuous periodic gust which only excited one distinct frequency. For a discrete gust, the reduction of 60% was obtained. It shall be noted that the relative reduction will be lower on a full aircraft, since some control authority needs to be reserved for primary flight control. The results support the use of μ-synthesis for designing controllers on aeroservoelastic systems.

Future work is suggested to examine the effect of weighting functions definition in μ-synthesis. Decoupling the influence of the individual weights would be desirable, and a more direct link between uncertainty definition and (disk-based) stability margins would be beneficial. The comparison study on controllers with different subsets of actuators and sensors could be expanded to investigate GLA systems with a minimal number of actuators and sensors. Future work will concentrate on applying the gust load alleviation technique in the transsonic speed regime, where aerodynamic non-linearities from pressure shocks or flow separation complicate the controller design.

Acknowledgments

The authors would like to thank all contributors involved in planning, preparation and execution of this wind tunnel experiment, making the active gust load alleviation test possible. Special thanks to Holger Mai and Marc Braune (test execution, measurement technology and data acquisition), Johannes Dillinger (wind tunnel model development and finite element modeling), Markus Ritter, Julius Sieg, and Martin Tang (aeroelastic identification of the model), Wolf R. Kruger (co-project lead of oLAF), and the wind tunnel team of the DNW-NWB.

References

[1] Binder, S., "Simultaneous Optimisation of Composite Wing Structures and Control Systems for Active and Passive Load Alleviation," PhD thesis, Delft University of Technology, Delft, Netherlands, 2021. https://doi.org/10.4233/uuid:fac93ccf-7e0b-4971-a797-d2617e378a1d.

[2] Regan, C. D., and Jutte, C. V., "Survey of Applications of Active Control Technology for Gust Alleviation and New Challenges for Lighter-Weight Aircraft," Technical Report, TM-2012-216008, NASA, 2012. URL https://ntrs.nasa.gov/citations/20120013450.

[3] Chin, J., "Universal-type gust alleviation system for aircraft," U.S. Patent 4905934. Grumman Aerospace Corporation., 1990. https://www.freepatentsonline.com/4905934.html.

[4] Fezans, N., Joos, H.-D., and Deiler, C., "Gust Load Alleviation for a Long-Range Aircraft With and Without Anticipation," *CEAS Aeronautical Journal*, Vol. 10, 2019, pp. 1033–1057. https://doi.org/10.1007/s13272-019-00362-9.

[5] Gangsaas, D., Ly, U., and Norman, D. C., "Practical Gust Load Alleviation and Flutter Suppression Control Laws Based on a LQG Methodology," *19th Aerospace Science Meeting*, AIAA, St. Louis, USA, 1981. https://doi.org/doi/10.2514/6.1981-21.

[6] Preumont, A., "Collocated Versus Non-Collocated Control," *Vibration Control Of Active Structures*, Springer, Dordrecht, 1997, Chap. 4, 1st ed., pp. 60–74. https://doi.org/10.1007/978-94-011-5654-7_46.

[7] Wang, X., van Kampen, E., Chu, Q. P., and De Breuker, R., "Flexible Aircraft Gust Load Alleviation with Incremental Nonlinear Dynamic Inversion," *Journal of Guidance, Control, and Dynamics*, Vol. 42, No. 7, 2019. https://doi.org/10.2514/1.G003980.

[8] Giesseler, H.-G., Kopf, M., Varutti, P., Faulwasser, T., and Findeisen, R., "Model Predictive Control for Gust Load Alleviation," *IFAC Proceedings Volumes*, Vol. 45, No. 17, 2012, pp. 27–32. https://doi.org/10.3182/20120823-5-NL-3013.00049.

[9] Skogestad, S., and Postlethwaite, I., *Multivariable Feedback Control*, 2nd ed., John Wiley & Sons, Chichester, UK, 2005.

[10] Doyle, J. C., Glover, K., Khargonekar, P. P., and Francis, B. A., "State-Space Solutions to Standard H_2 and H_∞ Control Problems," *IEEE Transactions on Automatic Control*, Vol. 34, No. 8, 1989. https://doi.org/10.1109/9.29425.

[11] Doyle, J. C., "Structured Uncertainty in Control System Design," *24th IEEE Conference on Decision and Control*, Fort Lauderdale, USA, 1985, pp. 260–265. https://doi.org/10.1109/CDC.1985.268842.

[12] Krüger, W. R., Mai, H., Kier, T., and Reimer, L., "Assessment of Active Load Control Approaches for Transport Aircraft - Simulation and Wind Tunnel Test," *International Forum on Aeroelasticity and Structural Dynamics (IFASD 2024)*, Den Haag, The Netherlands, 2024. URL https://elib.dlr.de/206124/.

[13] Dillinger, J., Mai, H., Krüger, W. R., Schmidt, T. G., and Stalla, F., "Design, Manufacturing and Identification of an Actively Controlled Flexible Wing for Subsonic Wind Tunnel Testing," *International Forum on Aeroelasticity and Structural Dynamics (IFASD 2024)*, Den Haag, The Netherlands, 2024. URL https://elib.dlr.de/205840/.

[14] Schmidt, T. G., Dillinger, J., Ritter, M., Altkuckatz, A., Hanke, C., Braune, M., Krüger, W. R., and Mai, H., "Design and Experimental Characterization of a Gust-Generator Concept with Rotating-Slotted Cylinders in the Low-Speed Wind Tunnel DNW-NWB," *International Forum on Aeroelasticity and Structural Dynamics (IFASD 2024)*, Den Haag, The Netherlands, 2024. URL https://elib.dlr.de/205804/.

[15] Stalla, F., Kier, T. M., Looye, G., and Pusch, M., "Aeroservoelastic Modeling and Robust Control for Gust Load Alleviation of an Experimental Wing," *AIAA SciTech 2024 Forum*, AIAA, Orlando, USA, 2024. https://doi.org/10.2514/6.2024-1442.

[16] Stalla, F., Looye, G., Kier, T. M., Michel, K., Ritter, M., Schmidt, T. G., Dillinger, J., and Tang, M., "Wind Tunnel Testing Active Gust Load Alleviation on an Experimental Wing," *International Forum on Aeroelasticity and Structural Dynamics (IFASD) 2024*, Den Haag, Netherlands, 2024. URL https://elib.dlr.de/205523/.

[17] Kier, T., and Looye, G., "Unifying Manoeuvre and Gust Loads Analysis Models," *International Forum on Aeroelasticity and Structural Dynamics (IFASD)*, Seattle, USA, 2009. URL https://elib.dlr.de/97798/.

[18] Hofstee, J., Kier, T., Cerulli, C., and Looye, G., "A Variable, Fully Flexible Dynamic Response Tool for Special Investigations (VarLoads)," *International Forum on Aeroelasticity and Structural Dynamics (IFASD)*, Amsterdam, Netherlands, 2003.

[19] Kier, T. M., and Hofstee, J., "VarLoads - eine Simulationsumgebung zur Lastenberechnung eines voll flexiblen, freifliegenden Flugzeugs," *Deutscher Luft- und Raumfahrtkongress (DLRK)*, DGLR, Dresden, Germany, 2004.

[20] Waszak, M. R., and Schmidt, D. K., "Flight Dynamics of Aeroelastic Vehicles," *Journal of Aircraft*, Vol. 25, No. 6, 1688, pp. 563–571. https://doi.org/10.2514/3.45623.

[21] Reschke, C., "Integrated Flight Loads Modelling and Analysis for Flexible Transport Aircraft," Ph.D. thesis, University of Stuttgart, Stuttgart, Germany, 2006. https://doi.org/10.18419/opus-3733.

[22] Guyan, R. J., "Reduction of Stiffness and Mass Matrices," *AIAA Journal*, Vol. 3, No. 2, 1964. https://doi.org/10.2514/3.2874.

[23] Rodden, W. P., and Johnson, E. H., *MSC/NASTRAN Aeroelastic Analysis User's Guide*, 2nd ed., MSC, 1994.

[24] Mauermann, T., "Flexible Aircraft Modelling for Flight Loads Analysis of Wake Vortex Encounters," Technical Report, DLR-FB 2010-37, German Aerospace Center (DLR), 2011. https://doi.org/10.24355/dbbs.084-201109120959-0.

[25] Beckert, A., and Wendland, H., "Multivariate Interpolation for Fluid-Structure-Interaction Problems Using Radial Basis Functions," *Aerospace Science and Technology*, Vol. 5, No. 2, 2001. https://doi.org/10.1016/S1270-9638(00)01087-7.

[26] Wright, J. R., and Cooper, J. E., *Introduction to Aircraft Aeroelasticity and Loads*, 2nd ed., Wiley, Chichester, UK, 2015. https://doi.org/10.1002/9781118700440.

[27] Roger, K. L., "Airplane Math Modeling Methods For Active Control Design," *AGARD Conference Proceedings 228*, Advisory Group For Aerospace Research and Development of NATO (AGARD), 1977.

[28] Karachalios, D. S., Gosea, I. V., and Antoulas, A. C., "The Loewner Framework for System Identification and Reduction," *Model Order Reduction*, De Gruyter, 2021, Chap. 6, pp. 181–228. https://doi.org/10.1515/9783110498967-006.

[29] European Union Aviation Safety Agency, *Certification Specification and Acceptable Means of Compliance for Large Aeroplanes (CS-25)*, Amendment 27, 2023. URL https://www.easa.europa.eu/en/certification-specifications/cs-25-large-aeroplanes.

[30] Tang, M., Böswald, M., Govers, Y., and Pusch, M., "Identification and Assessment of a Nonlinear Dynamic Actuator Model for Controlling an Experimental Flexible Wing," *CEAS Aeronautical Journal*, Vol. 12, 2021. https://doi.org/10.1007/s13272-021-00504-y.

[31] Theis, J., Pfifer, H., and Seiler, P., "Robust Modal Damping Control for Active Flutter Suppression," *Journal of Guidance, Control, and Dynamics*, Vol. 43, No. 6, 2020, pp. 1056–1068. https://doi.org/10.2514/1.G004846.

[32] Doyle, J., "Analysis of Feedback Systems with Structured Uncertainties," *IEE Proceedings, Pt. D, Control Theory and Applications*, Vol. 129, No. 6, 1982. https://doi.org/10.1049/ip-d.1982.0053.

[33] Doyle, J., Packard, A., and Zhou, K., "Review of LFTs, LMIs, and μ," *Proceedings of the 30th IEEE Conference on Decision and Control*, Vol. 2, Brighton, UK, 1991, pp. 1227–1232. https://doi.org/10.1109/CDC.1991.261572.

[34] Young, P. M., Newlin, M. P., and Doyle, J. C., "Practical Computation of the Mixed µ Problem," *1992 American Control Conference*, Chicago, USA, 1992, pp. 2190–2194. https://doi.org/10.23919/ACC.1992.4792521.

[35] Balas, G., Chiang, R., Packard, A., and Safonov, M., "Robust Control Toolbox User's Guide," Software Package Documentation, MATLAB R2024b, MathWorks Inc., 2024.

[36] Bennani, S., Looye, G., and Mulder, J. A., "RCAM Design Challenge Presentation Document: the µ-Synthesis Approach," Technical report TP-088-11, GARTEUR, 1997.

[37] Young, P. M., "Controller Design with Mixed Uncertainties," *Proceedings of the 1994 American Control Conference - ACC*, Vol. 2, Fort Lauderdale, USA, 1994, pp. 2333–2337. https://doi.org/10.1109/ACC.1994.752496.

[38] Young, P. M., "Controller Design with Real Parametric Uncertainty," *International Journal of Control*, Vol. 65, No. 3, 1996, pp. 469–509. https://doi.org/10.1080/00207179608921707.

[39] Fournier, H. et. al., "Robust Gust Load Alleviation of Flexible Aircraft Equipped with Lidar," *Journal of Guidance, Control, and Dynamics*, Vol. 45, No. 1, 2022. https://doi.org/10.2514/1.G006084.

[40] Reis, T., and Stykel, T., "Balanced Truncation Model Reduction of Second-Order Systems," *Mathematical and Computer Modelling of Dynamical Systems*, Vol. 14, No. 5, 2008. https://doi.org/10.1080/13873950701844170.

[41] Seiler, P., Packard, A., and Gahinet, P., "An Introduction to Disk Margins [Lecture Notes]," *IEEE Control Systems Magazine*, Vol. 40, 2020. https://doi.org/10.1109/MCS.2020.3005277.

[42] Kirmse, T., Boden, F., Meyer, R., and Philipp, F., "Wing Deformation Measurements for Manoeuvres of High Load at the Airbus A320 DLR-ATRA by Means of Image Pattern Correlation Technique," *European Test and Telemetry Conference*, Toulouse, France, 2021. URL https://elib.dlr.de/145368/.